Diagenetic evolution of fault zones in Urgonian microporous carbonates, impact on reservoir properties (Provence – SE France).

Irène Aubert [a], Philippe Léonide [a], Juliette Lamarche [a], Roland Salardon [a]

[a] Aix-Marseille Université, CNRS, IRD, Cerege, Um 34, 3 Place Victor Hugo (Case 67), 13331 Marseille Cedex 03, France

Microporous carbonate rocks form important reservoirs with permeability variability depending on sedimentary, structural and diagenetic factors. Carbonates are very sensitive to fluid-rock interactions that lead to secondary diagenetic processes like cementation and dissolution capable of modifying the reservoir properties. Focusing on fault-related diagenesis, the aim of this study is to identify impact of the fault zone on reservoir quality. This contribution focuses on two fault zones east to La Fare Anticline (SE France) cross-cutting Urgonian microporous carbonates. 122 collected samples along four transects orthogonal to fault strike were analysed. Porosity values have been measured on 92 dry plugs. Diagenetic elements were determined through the observation of 92 thin sections using polarized light microscopy, cathodoluminescence, carbonate staining, SEM and stable isotopic measurements ($\delta^{13}C$ and $\delta^{18}O$). Eight different calcite cementation stages and two micrite micro-fabrics were identified. As a main result, this study highlights that the two fault zones acted as drains canalizing low-temperature fluids at their onset, and induced calcite cementation which strongly altered and modified the local reservoir properties.

1. INTRODUCTION

Microporous carbonates form important reservoirs (Deville de Periere et al., 2017; Lambert et al., 2006; Sallier, 2005; Volery et al., 2009), with porosity values up to 35% (Deville de Periere et al., 2011). Due to their heterogeneous properties which depend on sedimentary, structural and diagenetic factors, microporous carbonates may determine a high variability of reservoir permeability (Bruna et al., 2015; Deville de Periere et al., 2011, 2017; Eltom et al., 2018; Florida et al., 2009; Hollis et al., 2010). Moreover, fault zones in carbonates play an important role on reservoir properties (Agosta et al., 2010, 2012; Caine et al., 1996; Delle Piane et al., 2016; Ferraro et al., 2019; Knipe, 1993; Laubach et al., 2010; Rossetti et al., 2011; Sinisi et al., 2016; Solum et al., 2010; Solum and Huisman, 2016; Tondi, 2007; Wu et al., 2019). Fault zones are complex structures composed of damage zones and the fault core encompassed by the host rock (Caine et al., 1996; Chester and Logan, 1986, 1987; Hammond and Evans, 2003). Faults can act as barriers (Agosta et al., 2010; Tondi, 2007), drains (Agosta et al., 2007, 2008, 2012; Delle Piane et al., 2016; Evans et al., 1997; Molli et al., 2010; Reches and Dewers, 2005; Sinisi et al., 2016; Solum and Huisman, 2016), or mixed hydraulic behaviour zones (Matonti et al., 2012) depending on their architecture and diagenetic evolution. Because of their hydraulic properties, fault zones influence the fluid flows in the upper part of Earth's crust (Bense et al., 2013; Evans et al., 1997; Knipe,

1993; Sibson, 1994; Zhang et al., 2008), and are capable of increasing the fluid-rock interactions. Carbonates are very sensitive to these interactions, which lead to diagenetic secondary processes like cementation and dissolution (Deville de Periere et al., 2017; Fournier and Borgomano, 2009; Lambert et al., 2006). Fault-related diagenesis locally modifies the initial rock properties (mineralogy and porosity), and therefore the reservoir properties (Hodson et al., 2016; Knipe, 1993; Knipe et al., 1998; Laubach et al., 2010; Woodcock et al., 2007). In case of a polyphasic fault zone, repeating fluid pathways-barriers behaviour in times leads to very complex diagenetic modifications. The initial vertical and lateral compartmentalization of microporous limestones is, therefore, accentuated by fault-related diagenesis. Hence, understanding faulting and diagenesis processes is crucial for a better exploration and production in carbonates. Urgonian microporous carbonates of Provence, are made of facies and reservoir properties analogue to Middle East microporous carbonate reservoirs (Thamama, Kharaib and Shuaiba Formations; Borgomano et al. 2002, 2013; Sallier 2005; Fournier et al. 2011; Leonide et al. 2012; Léonide et al. 2014). Although Urgonian microporous carbonates of Provence are analogue to Middle East reservoirs, the analogy can be extended to other faulted microporous carbonate reservoirs. To have a better comprehension of diagenetic modifications linked to fault zones in these rocks, the aim of this paper is (i) to determine the diagenetic evolution of polyphasic fault zones; (ii) to identify their impact on reservoir properties and (iii) to link the fault evolution with the fluid flow and geodynamic history of the basin.

2. GEOLOGICAL CONTEXT

We studied two faults cross-cutting microporous Valanginian-to-Early Aptian Urgonian carbonates of the South-East Basin (Provence-SE France) deposited along the southern margin of the Vocontian Basin (Léonide et al., 2014; Masse and Fenerci Masse, 2011). The "Urgonian" platform carbonates (Masse, 1976) reached their maximum areal extension during the late Hauterivian–Early Aptian (Masse and Fenerci-Masse, 2006). From Albian to Cenomanian, the regional Durancian uplift triggered exhumation of Early Cretaceous carbonates, bauxitic deposition (Guyonnet-Benaize et al., 2010; Lavenu et al., 2013; Léonide et al., 2014; Masse and Philip, 1976; Masse, 1976), and development E-W-trending extensional faults (Guyonnet-Benaize et al., 2010; Masse and Philip, 1976). During Late Cretaceous times, platform environment led to a transgressive rudist deposition (Philip, 1970). From Late Cretaceous to Eocene, the convergence between Iberia and Eurasia plates (e.g. Bestani 2015, and references therein) caused a regional N-S shortening (e.g. Molliex et al. 2011 and references therein). The so-called "Pyrénéo-Provençal" shortening, gave rise to E-W-trending north-verging thrust faults and ramp folds (e.g. Bestani et al. 2016, and references therein). From Oligocene to Miocene, the area underwent extension associated to Liguro-Provençal Basin opening (e.g. Demory et al. 2011). During Mio-Pliocene times, the Alpine shortening dimly impacted the studied area (Besson, 2005; Bestani, 2015), and reactivated the "Pyrénéo-Provençal" structures (Champion et al., 2000; Molliex et al., 2011).

We studied two faults pertaining to a Km-scale fault system on the E-W-trending La Fare anticline near Marseille (Fig. 1A). The southern limb of this anticline dips 25° S, and is constituted by Upper Hauterivian, Lower Barremian and Santonian rocks (Fig. 1B). The Upper Barremian carbonates are composed, from bottom to top, of a 120 m-thick calcarenitic unit with cross-beddings, a 40 m-

thick massive coral-rich calcarenite unit, and an upper 10 m-thick calcarenite unit (Masse, 1976; Matonti et al., 2012; Roche, 2008). Santonian age coarse rudist limestones uncomfortably overlap the Barremian carbonates (Fig. 1A).

The Castellas fault zone is a 2.14 km-long left-lateral strike-slip fault, N060° to 070°-trending and 40° to 80°N-dipping (Fig. 2A, 2B; table 1) composed of horse structures, secondary faults and lenses (Fig. 2A, 2C; Aubert et al. (2019b)). The second investigated fault zone "D19" is composed of 5 sub-fault zones (F1 to F5) restricted in a 50 m-long interval (Fig. 2E, 2H; Table 1; (Aubert et al., 2019a)). Sub-faults are organised into two sets. The first one comprises F3 and F4, N040 to N055-trending, 60-80°NW-dipping (orange traces on Fig. 2F). Set 2 is N030-trending, dipping 80°E, with left-lateral strike-slip slickensides pitch 20° to 28°SW (F1, F2, F5, red traces on Fig. 2F).

The internal structure of both fault zones results from three distinct tectonic events:

- the Durancian uplift dated as mid-Cretaceous leading to extension and to normal *en echelon* normal faults. The Castellas fault nucleated during this first extensional event and bears early dip-slip normal striations (Matonti et al., 2012),
- the Early Pyrenean compression with N000° to N170°-trending σ_H (see cited references in Espurt et al. 2012) which reactivated the Castellas fault as sinistral (Matonti et al., 2012) and led to the newly-formed strike-slip faults of the D19 outcrop (Aubert et al., 2019a).
- the Pyrenean to Alpine folding, triggering the 25°S tilting of the strata and fault zones. Faults of the D19 outcrop were reactivated while the Castellas fault tilting led to an apparent present-day reverse throw (Aubert et al., 2019a).

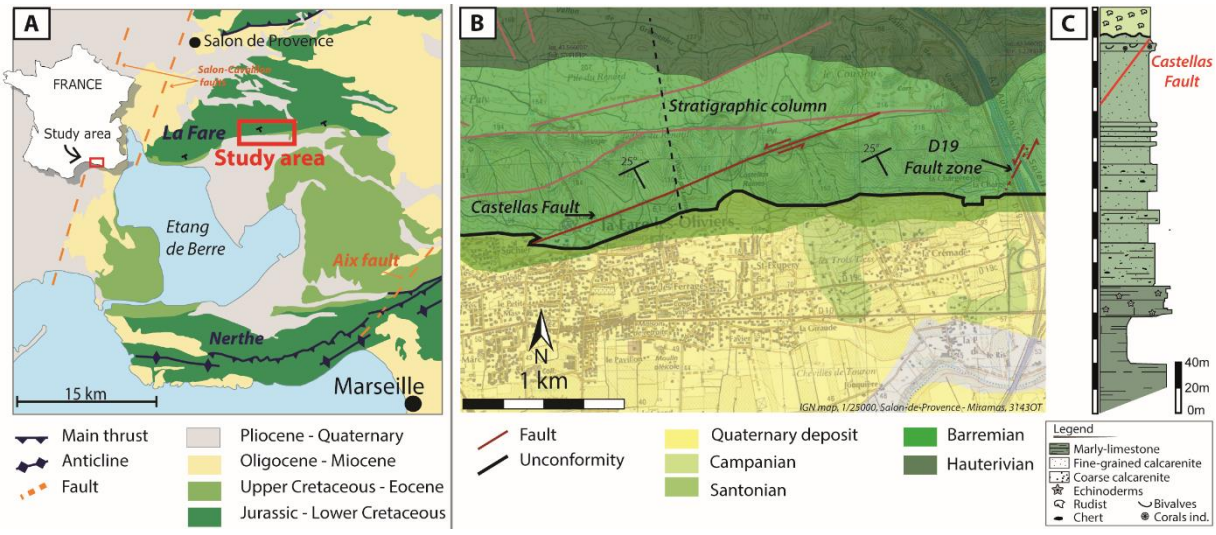

Figure 1 *: Geological context of the study area. A: geological map of Provence, B: Simplified structural map with the location of the Castellas fault and the stratigraphic column (black dashed line); C: Stratigraphic column of exposed Cretaceous carbonates (modified from Roche, 2008).*

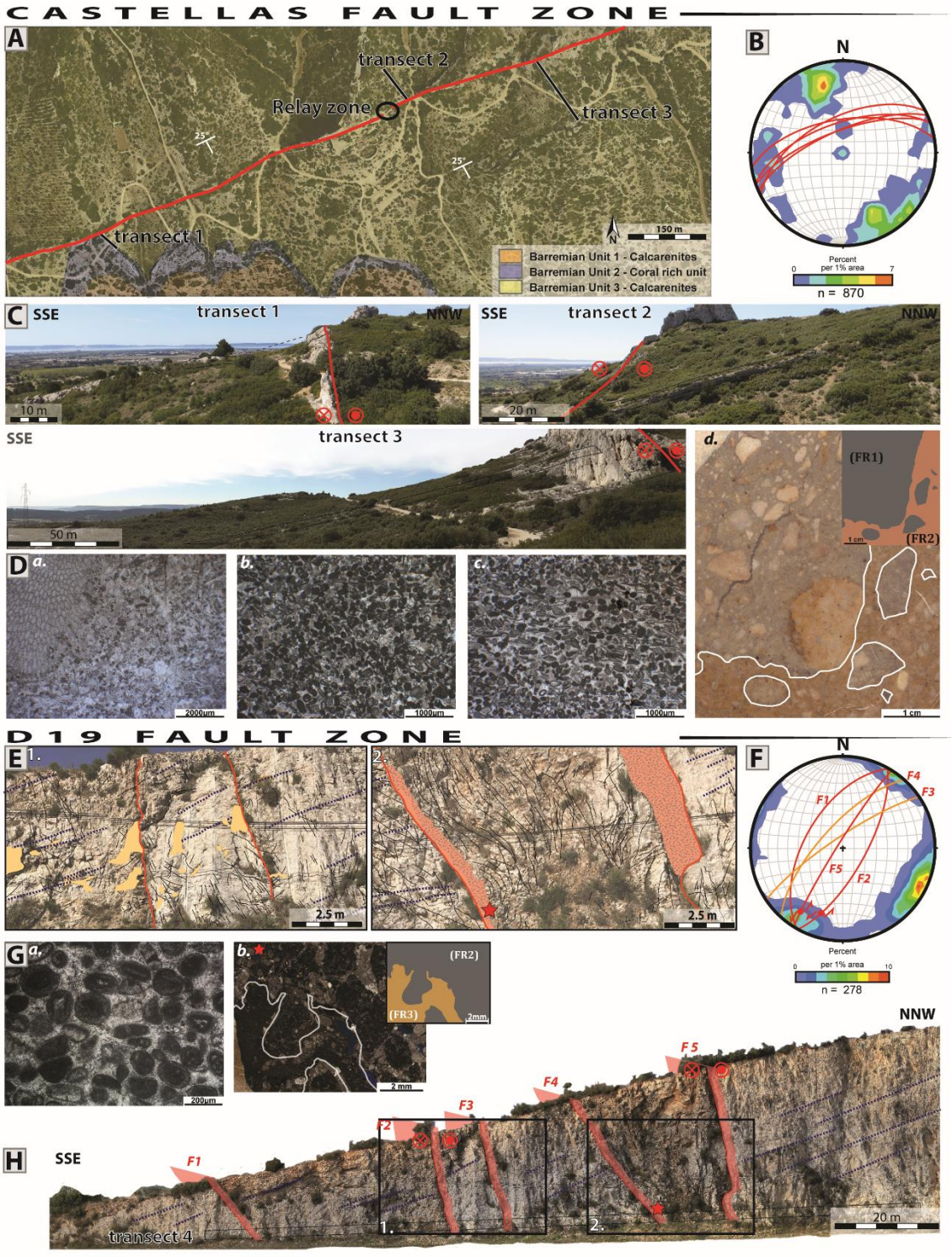

Figure 2 *: A: Castellas fault map on aerial photo with position of the studied transects and the relay zone; B: stereographic projection of poles to fractures (density contoured) and faults (red lines)* (Allmendinger et al., 2013; Cardozo and Allmendinger, 2013)*; C: Photos of transects 1 to 3; D: Photomicrographs of carbonate host-rock facies (a) transect 1 coral rich unit, (b) transect 2 calcarenites, (c) transect 3 calcarenites and (d) fault rocks 1 and 2 (FR1 and FR2); E: Pictures of D19 outcrop F: Stereographic projection of poles to fractures (density contoured), set one faults (orange line) and set 2 faults (red line) G: Photomicrographs of host rock facies (a) and of fault rocks (b; red stars on the pictures); H: D19 outcrop including the five faults F1 to F5.*

***Table 1**: structural properties of the fault zones.*

Fault zones	Fault	Direction	Dip	Dip direction	Pitch striation	Fault core thickness	Fault Rocks		
							FR1	FR2	FR3
Castellas	Castellas	060 - 070	40 to 80	N	14 W -	0 to 4 m	sparsely present	majoritarely present	/
D19	F1	030	56	W		20	/	<10 cm	/
	F2	029	70	E	28 S	10 to 15	/	?	variable thickness
	F3	056	80	N		0 to 15	/	?	?
	F4	042	70	W		20	/	in the clasts of FR3	variable thickness
	F5	032	85	N	20 SW	50 to 100	/	/	variable thickness

3. DATA BASE

We performed 4 transects across the Castellas Fault and the D19 Fault (Fig. 2). Transect 1 is located along the coral rich unit 2. This lithostratigraphic unit is essentially composed of peloidal grains and bioclasts (corals, bivalves and stromatoporidae; Fig. 2Da). Transects 2 and 3 cross-cut unit 3, made of fine calcarenites with peloidal grains and a rich fauna (foraminifera, bivalves, ostracods and echinoderms; Fig. 2Db, c). Transect 4 was conducted along the D19 outcrop (Fig. 3), which exposes Barremian outer platform bioclastic calcarenite with current ripples. The grains are mainly peloids with minor amounts of bioclasts (solidary corals, bryozoans, bivalves and some rare miliolids; Fig. 2Ga).

The different tectonic events impacted the fault zone and fault core structure. Three different fault rock types were identified in the fault core of the two investigated fault zones (see Aubert et al. 2019a; Matonti et al., 2012). Fault rock 1 (FR1) results from the extensional activation of the Castellas fault during Durancian uplift. It is a cohesive breccia composed of sub-rounded to rounded clasts from the nearby damage zone and <30% of fine-grey matrix (Fig. 2Dd). Fault rock 2 (FR2), is linked to the strike-slip reactivation of the Castellas fault and to the onset of D19 fault zone during the Pyrenean shortening. FR2 presents two morphologies depending on the fault zones. Within Castellas fault, FR2 is an un-cohesive breccia with an orange/oxidized matrix with angular to sub-rounded clasts belonging to the nearby damage zone and from FR1 (Fig. 2Dd). In the D19 fault zone, FR2 is a cohesive breccia with rounded clasts of the damage zone and a white cemented matrix (Fig. 2Gb). Fault rock 3 (FR3) is formed by the reactivation of D19 fault zone. The timing of D19 fault reactivation is tricky to determine as it can be related both to Pyrenean or alpine shortening. FR3 is composed of angular to sub-angular clasts from FR2 and from the nearby damage zone dispersed in an orange/oxidized matrix (<20%) (Fig. 2Gb).

4. METHODS

The data set comprises 122 samples, 62 from Castellas and 60 from D19 outcrops, collected along the 4 transects. Porosity values were measured on 92 dry plugs with a Micromeritics AccuPyc 1330 helium pycnometer. Microfacies were determined on 92 thin sections. Impregnation with a blue-epoxy resin allowed us to decipher the different pore types. Thin sections were coloured with a solution of hydrochloric acid, Alizarin Red S and potassium ferricyanide to distinguish carbonate

minerals (calcite and dolomite). Thin sections were analysed using cathodoluminescence to discriminate the different generations of calcite cements. The paragenetic sequence was defined based on superposition and overlap principles observed on thin sections using a Technosyn Cold Cathode Luminescence Model 8200 Mk II coupled to an Olympus_BH2 microscope and to a Zeiss_MR C5. Micrite micro-fabric and major element composition of two samples from the fault zone, two from the host rock and 1 from the D19 karst infilling were measured using PHILIPS XL30 ESEM with a beam current set at 20 kV on fresh sample surfaces and on thin sections. To determine stable carbon and oxygen isotopes ($\delta^{13}C$ and $\delta^{18}O$), 204 microsamples (<5 mg) were drilled, 194 of them were micro-drilled from polished thin sections with an 80 µm diameter micro-sampler (Merkantec Micromill) at the VU University (Amsterdam, The Netherlands). We micro-sampled bulk rocks (57), sparitic cements (101), fault rocks (9) and micrite (27). The bulk rock values are related to a non-selective sampling giving information on the whole rock isotopic values. These values do not capture the signature of isolated cement (Swart, 2015). Carbon and oxygen isotopic values were acquired with Thermo Finnigan Delta + mass spectrometer equipped with a GASBENCH preparation device at VU University Amsterdam. The internationally used standard IAEA-603, with official values of +2.46‰ for $\delta^{13}C$ and -2.37‰ for $\delta^{18}O$, is measured as a control standard. The standard deviation (SD) of the measurements is respectively < 0.1‰ and < 0.2 ‰ for $\delta^{13}C$ and $\delta^{18}O$,. Ten whole rock samples were analysed using a Gasbench II connected to a Thermo Fisher Delta V Plus mass spectrometer at the FAU University (Erlangen, Germany). Measurements were calibrated by assigning $\delta^{13}C$ values of +1.95‰ to NBS19 and -47.3‰ to IAEA-CO9 and $\delta^{18}O$ values of -2.20‰ to NBS19. All values are reported in per mil relative to V-PDB.

5. RESULTS

1. MICROPOROSITY AND POROSITY

Porosities measured on the 92 samples show a strong decrease towards the fault core (Fig. 3): dropping from more than 10% in the host carbonates (mean: 15%, SD: 2.68 for Castellas and mean: 12.3%, SD: 2.52 for D19) to less than 5% within fault zones (mean: 4.8%, SD: 2.07 for Castellas and mean: 3.16%, SD: 2.35 for D19).

Along transects, some porosity variations occur as follows:

- North of the Castellas fault, along the 60 m-long transect 2 the porosity is constantly lower than 7% (mean of 4.4%, SD: 1.53; Fig. 3A).
- South of the Castellas fault, the reduced porosity zone is wider than 40 m in transect 3 and 30 m in transect 1 (Fig. 3A). In a 10 m-thick zone from the fault plane, porosity reduction occurs with lower values in transect 1 (average 4.9%) than in transect 3 (average 5.6%).
- In the D19 fault zone, the lowest porosity values are found in narrow zones around the faults (less than 2 m-wide) and in the lens between F4 and F5. Though, this porosity decrease is not homogeneous in fault zone and high values are found north of F1 and F3 (Fig. 3B).

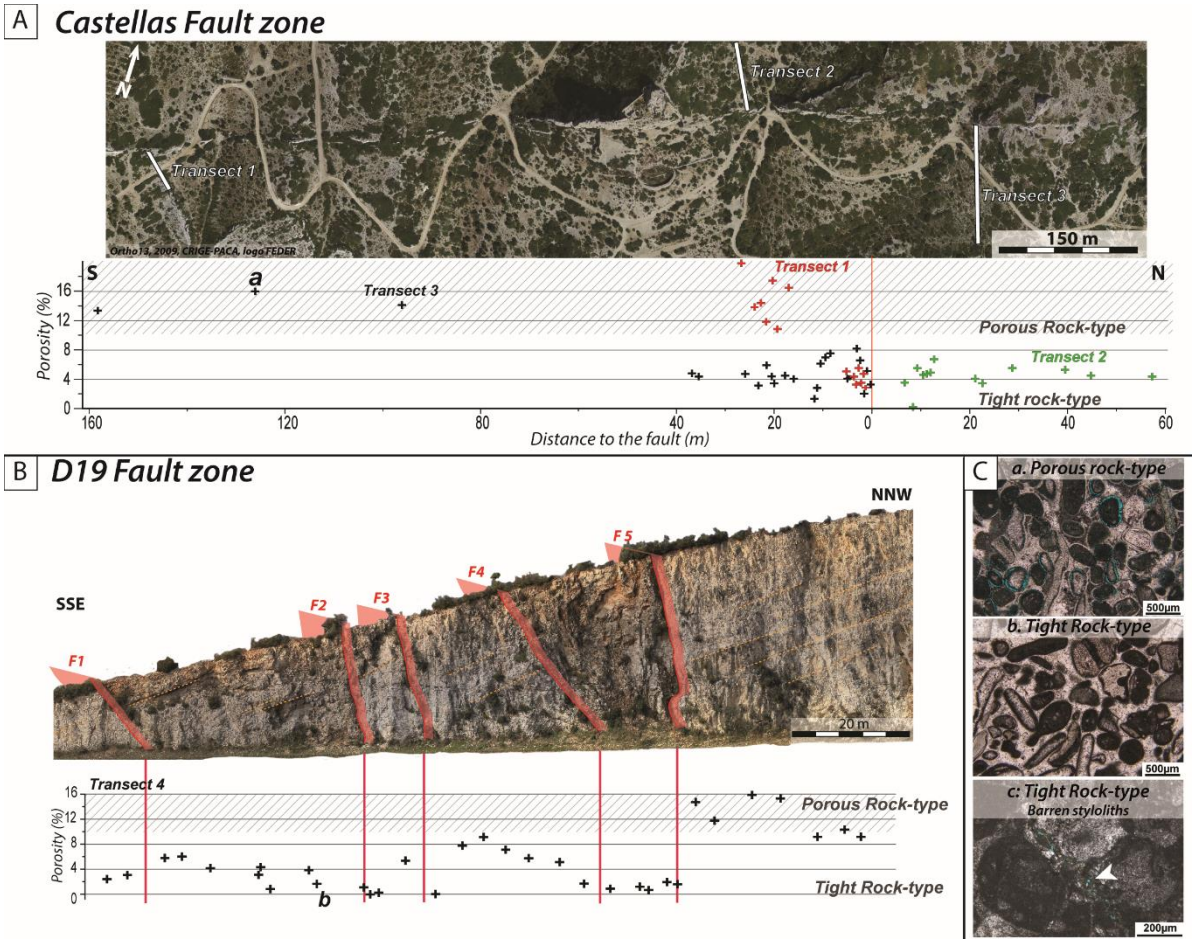

***Figure 3**: A: Castellas fault zone aerial view (Ortho13, 2009, CRIGE-PACA, logo FEDER) and porosity values measured along transect 1 (red Cross), transect 2 (green cross) and transect 3 (black cross); B: porosity values measured along D19 fault zone; C: Pore types in the host rock (a) and in the fault zones (b and c).*

Microscope observation of thin sections impregnated with blue-epoxy resin allowed to identify a porous rock-type with ϕ>10% mainly in micritized grains as microporosity and moldic porosity (Fig. 3Ca), and a tight rock-type with ϕ< 5%, where the porosity is mostly linked to barren stylolites (Fig. 3Cb, c).

2. DIAGENETIC PHASES

a. Micrite micro-fabric

Micritised bioclasts, ooids and peloids were observed after SEM analysed of two fault zones samples and two host rock samples. Two micro-fabrics of micrite occur with specific crystal shape, sorting and contacts according to Fournier et al. (2011). Within both fault zones, the micrite is tight, with compact subhedral mosaic crystals less than 10 µm-wide (MF1; Fig. 4A, B). In the host rock, the micrite is loosely packed, and partially coalescent with puntic rarely serrate, subhedral to euhedral crystals less than 5 µm-wide (MF3; Fig. 4C, D, E). MF1 correlates with low porosity values (< 5%), while MF3 with higher porosity (> 10%).

b. Diagenetic cements

Eight different cement stages were identified (Fig. 5). The red stain links to Alizarin Red S coloration and shows that all visible cements are made of calcite, which exhibits variable characteristics (morphology, luminescence, size and location).

The first two cement phases occur in both fault zones. The first cement (C0) is non-luminescent isopachous calcite of constant thickness (~10 μm) around grains (Fig. 5A). The second cement (C1) is divided in two sub-phases: a non-luminescent calcite, C1a, with a crystal size ranging from 50 μm to more than 200 μm, a dog-tooth morphology in intergranular spaces, and a bright luminescence calcite, C1b, covering C1a with a maximum thickness of 100 μm (Fig. 5A, B, D, G). C1b also fills micro-porosity in micritised grains (Fig. 5B). C1b areal occurrence strongly increases in Castellas fault zone.

Five cements or replacive phases extensively occur in the Castellas sector and rarely in the D19 outcrop:

- C2 is a sparitic cement, with dull-orange luminescent crystals with a maximum size of 100 µm only found in veins of the fault core (Fig. 5B). SEM measurements show the presence

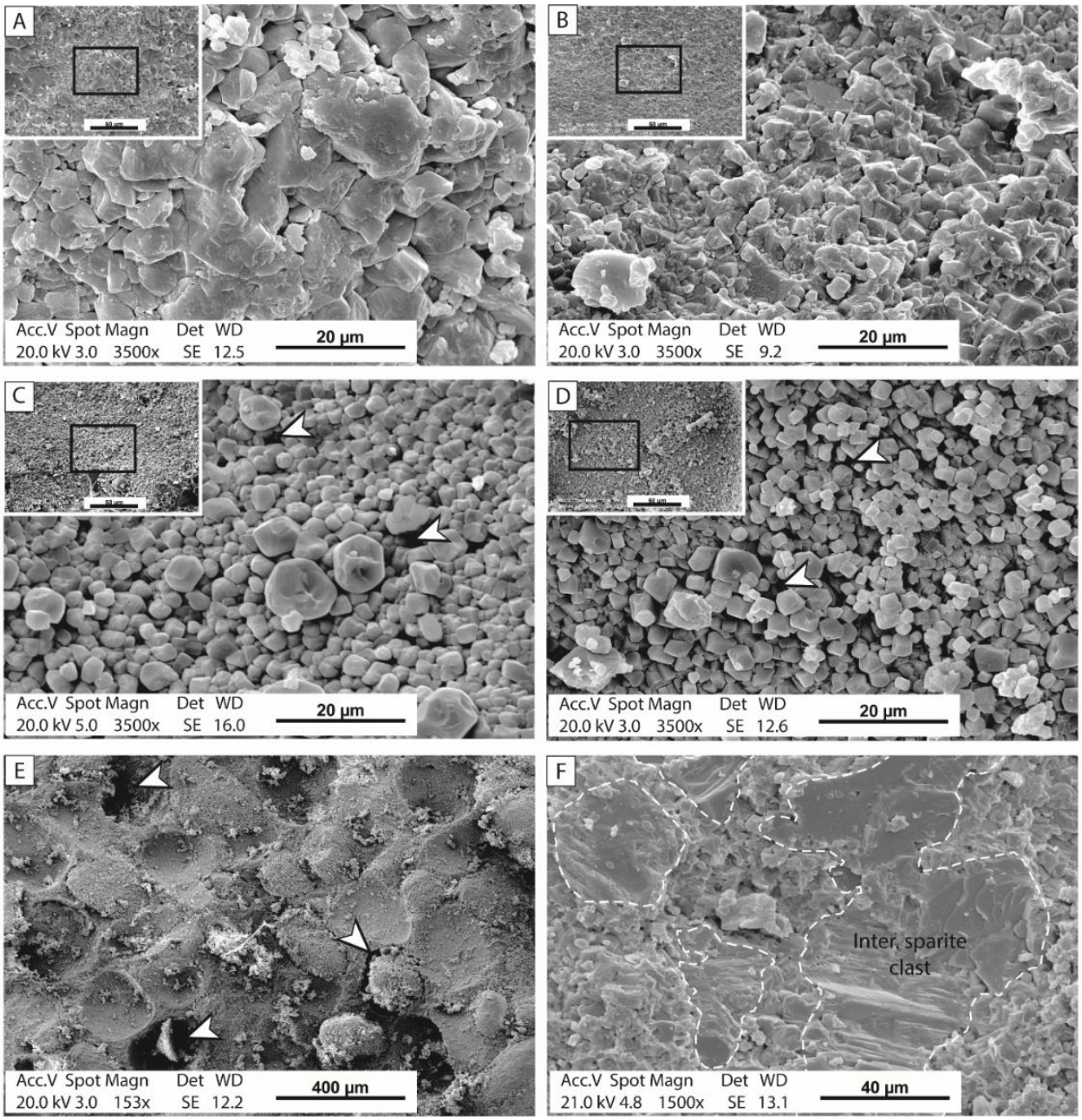

Figure 4 *: MEB pictures of micrite micro-fabric and microporosity (white arrows); A. MF1 micrite micro-fabric in Castellas fault zone (2.5 m to fault plane); B: MF1 micrite micro-fabric within D19 fault zones (2 m away from F5 fault plane); C: MF3 micrite micro-fabric within Castellas host rock (188 m away from the fault plane); D: MF3 micrite micro-fabric within D19 host rock (95 m away from F5 fault plane); E: D19 host rock moldic porosity; F: Karst infilling.*

222 of Si and Al in the C2 veins. Most of Si crystals are automorphic and have black
223 luminescence.

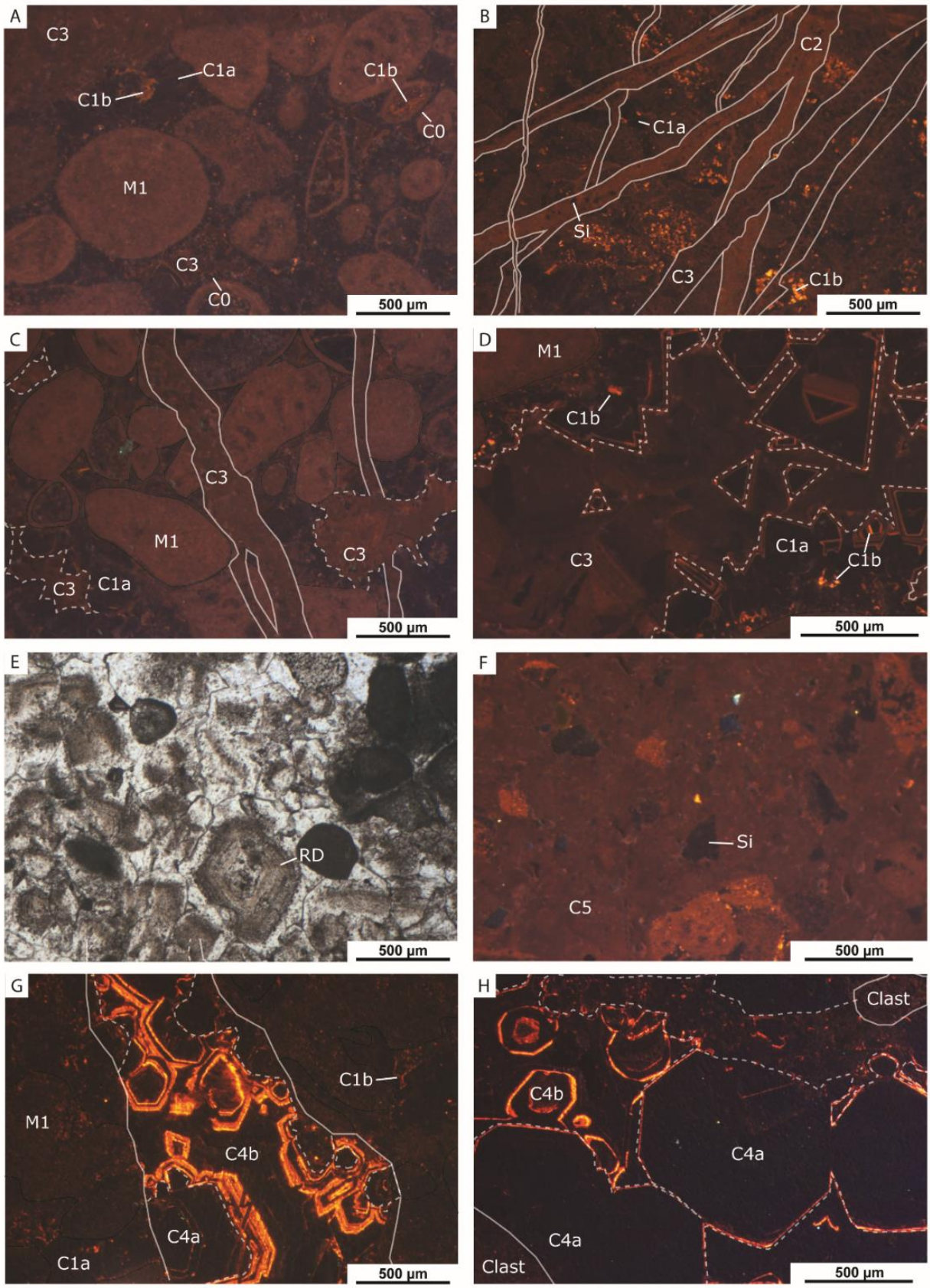

Figure 5 *: Thin-sections under cathodoluminescence; A: Calcarenite in transect 3 with micritised grain (M1), and intergranular volume cemented with C1 a and b and C3; B: C2 (with Si) and C3 veins affecting Castellas FR1 clasts with micritsed grains cemented by C1b; C: C3 veins, cements and intergranular volumes in Castellas fault zone; D: C1 (a and b) and C3 cementing moldic porosity of transect 3 calcarenite; E: FR1 matrix with phantom of cloudy appearance replacive dolomite (RD); F: FR1 matrix de-dolomitized by C5 containing quartz grains; G: C4 (a and b) cementing vein of D19 fault zone; H: matrix of D19 FR2 cemented by C4 (a and b).*

- C3 is a blocky calcite with non to red-dull luminescence in veins, moldic and intergranular pores (Fig. 5B, C, D). This cement also occurs in few veins of D19 sectors but is not restricted only to the fault zone.
- Phantoms of planar-e (euhedral) dolomite crystals (Sibley and Gregg, 1987) with a maximum size of 500 µm affect the matrix of FR1 (Fig. 5E). They are vestiges of a previous dolomitization phase. They have a cloudy appearance caused by solid micritic inclusion inside crystals and can be considered as replacive dolomite (RD; Machel, 2004). Within the FR1 matrix, an important concentration of angular grains of quartz with a maximum size of 300 µm is noticed (Fig. 5F).
- A blocky calcite C4 (referred to as S2 in Aubert et al. (2019a)) is mainly present in veins of the D19 outcrop, in matrix of FR2, and intergranular and moldic pores (Fig. 5G, H). This cement shows zonations of non-luminescent and bright luminescent bands and can be divided in two sparitic sub-phases: C4a which is non-luminescent with some highly luminescent bands while C4b is bright luminescent with some thin non-luminescent zones. C4a occurs in lesser proportion in some veins along transect 2 and 3 of the Castellas fault.
- A sparitic cement C5, with a red-dull luminescence replaces the RD phase (Fig. 5F).

c. Additional diagenetic features

In addition to cementation phases, other diagenetic elements affected both fault zones. Karst infilling occurs in the F2 fault zone of the D19 outcrop. It is composed of well-sorted grains deposited in laminated layers. This karst deposit presents a stack of alternating micrite-rich and grain-rich layers from the latter composed of former blocky calcite belonging to dissolved grainstones. The laminated layers are affected by veins and stylolites; some of these are deformed due to the grain fall on sediments. Micritic layers have been observed under SEM, and the micrite appears tight with compact subhedral mosaic crystals (Fig. 4F). We observed oxide filling mainly in the Castellas area in dissolution voids affecting C1a, C1b and C3 cementation phases and in D19 in karstic fill. The areal amount of oxides increases close to stylolites.

3. CARBON AND OXYGEN ISOTOPES

Isotope measurements were realized on samples collected along transects of the fault zones. A hundred and eighty-nine measurements of C and O isotopes were performed on 16 samples and 32 thin sections (Fig. 6A, table 2).

Sampling was done in bulk rock (66), sparitic cement (101; veins, intergranular volume and fault rock cements) and in fault rocks (10) in order to determine their isotopic signature. Isotopic values range from -10.40‰ to -3.65‰ for $\delta^{18}O$ and from -7.20‰ to +1.42‰ for $\delta^{13}C$ (Fig. 6A, B, table 2). The bulk rock values range from -9.18‰ to -4.34‰ for $\delta^{18}O$ and from -4.80‰ to +1.19‰ for $\delta^{13}C$ (Fig. 6A, table 2). These values are split in two sets. Set 1 includes transects 1 and 3 of the Castellas Fault. Bulk values range from -6.07‰ to -4.34‰ for $\delta^{18}O$ and from -1.41‰ to +1.19‰ for $\delta^{13}C$. Set 2 includes transects 2 (Castellas) and 4 (D19). Bulk values range from -9.18‰ to -5.20‰ for $\delta^{18}O$ and from -4.80‰ to -0.60‰ for $\delta^{13}C$ (Fig. 6B, table 2). In transect 3, the isotopic values only slightly vary, ranging from -6.13‰ to -4.50‰ for $\delta^{18}O$ and from -1.41‰ to +0.47‰

for $\delta^{13}C$ respectively (Fig. 6C, table 2). On the contrary, values are more variable along the D19 transect; they range from -9.18‰ to -5.20‰

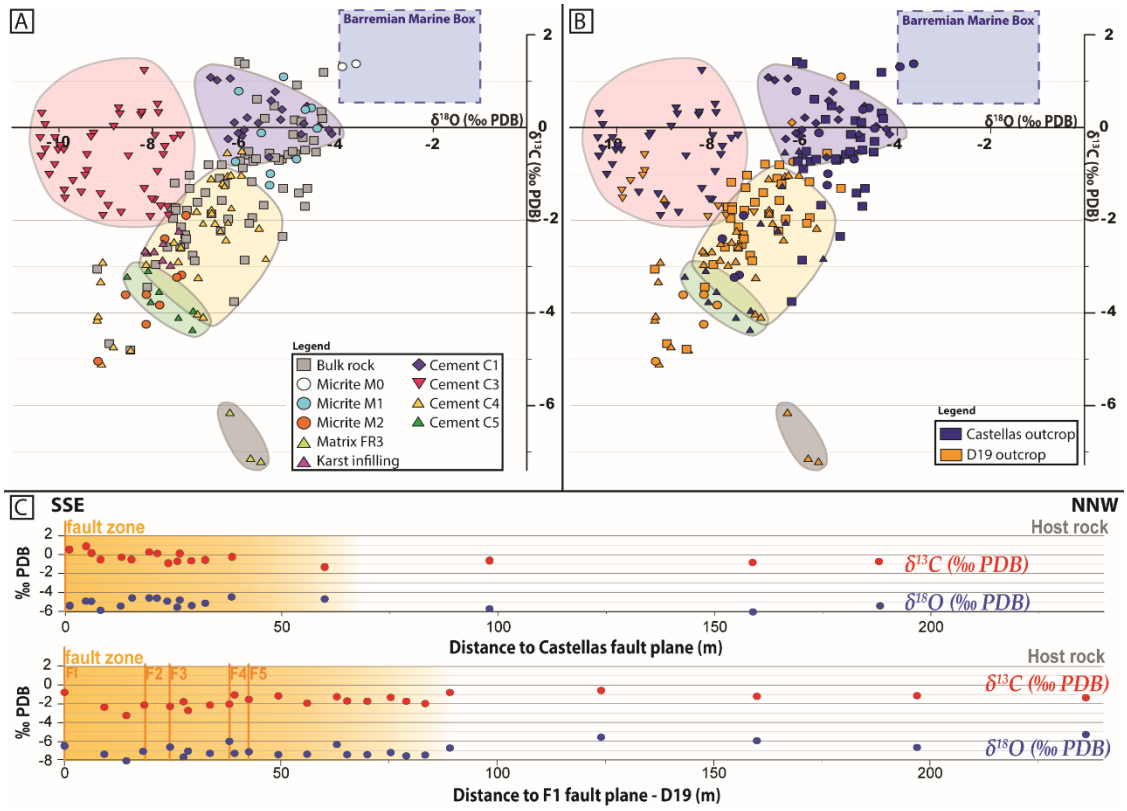

Figure 6 *: Isotopic values of $\delta^{13}C$ and $\delta^{18}O$ measured on bulk rock, cement phases, and micrite. Range values of "Urgonian marine box" from Moss & Tucker (1995) and Godet et al. (2006); A: set of values sorted by the nature of diagenetic phases and B: values sorted by the fault zone; C: lateral evolution of $\delta^{13}C$ and $\delta^{18}O$ bulk isotopic values in Castellas (top) and in D19 (bottom) fault zones.*

for $\delta^{18}O$ and from -4.80‰ to -0.60‰ for $\delta^{13}C$ (Fig. 6C, table 2). The $\delta^{13}C$ values are more depleted approaching to faults, especially south of F2.

Isotopic values of cements filling veins, intergranular volumes, karst infillings, and fault rocks are divided into 5 groups (Fig. 6A, table 2):

- Isotopic values of C1 cement fluctuate from -6.76‰ to -4.45‰ for $\delta^{18}O$ and from -1.28 to +1.08‰ for $\delta^{13}C$;
- Isotopic values of C3 cement range from -10.40‰ to -6.73‰ for $\delta^{18}O$ and from -2.09 to +1.22‰ for $\delta^{13}C$;
- Isotopic values of C4 cement in FR1 and FR2 matrix and in karst infillings range from -9.18‰ to -4.60‰ for $\delta^{18}O$ and from -5.10‰ to -0.74‰ for $\delta^{13}C$ with a positive covariance between $\delta^{18}O$ and $\delta^{13}C$. FR2 matrix values (from -7.06‰ to -6.55‰ for $\delta^{18}O$ and from -1.10 to -2.24‰ for $\delta^{13}C$) present slightly less depleted values than karst infillings with mean values of -7.83‰ and -2.53‰ for $\delta^{18}O$ and $\delta^{13}C$ respectively. (Fig. 6A). In the Castellas

fault, 4 isotopic values from two veins are enriched with means of -6.25 and -4.2‰ for $\delta^{18}O$ -0.64 and -0.09‰ for $\delta^{13}C$ having similar positive covariance than the other C4 values;

- Isotopic values of C5 cement, sampled in FR1 matrix display mean of -7.49‰ for $\delta^{18}O$ and -4.01‰ for $\delta^{13}C$ (Fig. 6A);
- Isotopic values of FR3 matrix with a mean of -5.98‰ for $\delta^{18}O$ and -6.83‰ for $\delta^{13}C$ (Fig. 6A).

Table 2*: Carbon and oxygen isotope values of bulk carbonates for Castellas fault zone and D19 fault zones. B: bulk measurement; M: micrite value; C1, C3, C4, C5: cement isotopic value; FR: fault rock isotopic value.*

Transect	Sample	$\delta^{13}C$ (‰VPDB)	$\delta^{18}O$ (‰VPDB)	Class	Distance to F. (m)
Transect 1 (Cast.)	201	1,19	-4,34	B	1,3
Transect 1 (Cast.)	201	1,02	-6,62	C1	1,3
Transect 1 (Cast.)	201	1,31	-3,94	M	1,3
Transect 1 (Cast.)	201	1,37	-3,65	M	1,3
Transect 1 (Cast.)	213	-0,68	-5,24	B	22,7
Transect 1 (Cast.)	213	-0,58	-5,10	B	22,7
Transect 1 (Cast.)	213	-0,18	-6,09	C1	22,7
Transect 1 (Cast.)	213	0,03	-4,45	C1	22,7
Transect 1 (Cast.)	213	0,09	-4,77	C1	22,7
Transect 1 (Cast.)	213	-2,09	-6,92	C4	22,7
Transect 1 (Cast.)	213	-0,68	-4,92	M	22,7
Transect 2 (Cast.)	c3b17	-0,52	-5,95	B	4,6
Transect 2 (Cast.)	c3b17	-2,07	-6,38	C4	4,6
Transect 2 (Cast.)	c3b7	-0,64	-5,51	B	9,3
Transect 2 (Cast.)	c3b26	-3,76	-6,26	B	22,6
Transect 2 (Cast.)	c3b26	-2,85	-5,58	C4	22,6
Transect 2 (Cast.)	c3b26	-1,31	-4,69	B	57,3
Transect 2 (Cast.)	c3b7	-1,76	-6,31	C1	57,3
Transect 2 (Cast.)	c3b7	-1,28	-6,46	C1	57,3
Transect 2 (Cast.)	c3b26	-2,35	-5,22	M	57,3
Transect 2 (Cast.)	c3b26	-1,70	-4,75	M	57,3
Transect 3 (Cast.)	327	-0,24	-7,55	C3	0,3
Transect 3 (Cast.)	325	-1,90	-9,06	C3	0,3
Transect 3 (Cast.)	325	-1,69	-8,95	C3	0,3
Transect 3 (Cast.)	327	-3,11	-8,09	C4	0,3
Transect 3 (Cast.)	327	0,47	-5,40	B	1,0
Transect 3 (Cast.)	327	-0,18	-7,95	C3	1,0

Transect 3 (Cast.)	327	-0,17	-7,41	C3	1,0
Transect 3 (Cast.)	328	0,10	-5,74	C1	1,6
Transect 3 (Cast.)	328	-1,32	-8,18	C3	1,6
Transect 3 (Cast.)	328	-0,59	-7,77	C3	1,6
Transect 3 (Cast.)	328	-0,42	-7,74	C3	1,6
Transect 3 (Cast.)	328	-0,13	-9,26	C3	1,6
Transect 3 (Cast.)	328	0,02	-8,83	C3	1,6
Transect 3 (Cast.)	328	0,29	-8,70	C3	1,6
Transect 3 (Cast.)	328	0,42	-8,73	C3	1,6
Transect 3 (Cast.)	328	0,50	-7,89	C3	1,6
Transect 3 (Cast.)	328	1,22	-8,18	C3	1,6
Transect 3 (Cast.)	333	-1,84	-8,67	C3	1,6
Transect 3 (Cast.)	333	-0,96	-7,89	C3	1,6
Transect 3 (Cast.)	328	-0,14	-4,17	C4	1,6
Transect 3 (Cast.)	328	-0,05	-4,23	C4	1,6
Transect 3 (Cast.)	329	0,16	-4,95	B	2,4
Transect 3 (Cast.)	333	-0,25	-6,38	C1	4,6
Transect 3 (Cast.)	333	-0,12	-6,17	C1	4,6
Transect 3 (Cast.)	333	-0,62	-8,52	C3	4,6
Transect 3 (Cast.)	333	-0,12	-5,67	M	4,6
Transect 3 (Cast.)	333	-0,02	-4,48	M	4,6
Transect 3 (Cast.)	333	0,42	-4,60	M	4,6
Transect 3 (Cast.)	337	0,19	-5,59	B	9,5
Transect 3 (Cast.)	302	-0,53	-4,50	B	11,8
Transect 3 (Cast.)	302	-0,49	-4,74	B	11,8
Transect 3 (Cast.)	302	-0,62	-10,38	C3	11,8
Transect 3 (Cast.)	302	-0,49	-10,02	C3	11,8
Transect 3 (Cast.)	305	0,33	-4,38	B	16,0
Transect 3 (Cast.)	306	0,21	-4,35	B	17,8
Transect 3 (Cast.)	307	-0,01	-4,46	B	18,2
Transect 3 (Cast.)	308	-0,57	-4,95	B	20,0
Transect 3 (Cast.)	308	-1,44	-9,11	C3	20,0
Transect 3 (Cast.)	308	-0,23	-10,40	C3	20,0
Transect 3 (Cast.)	308	-0,22	-10,08	C3	20,0
Transect 3 (Cast.)	309	-1,41	-4,87	B	20,5
Transect 3 (Cast.)	309	-0,52	-5,01	B	20,5
Transect 3 (Cast.)	309	-0,15	-4,82	C1	20,5
Transect 3 (Cast.)	309	-1,56	-7,96	C3	20,5
Transect 3 (Cast.)	309	-1,55	-8,01	C3	20,5
Transect 3 (Cast.)	312	0,12	-4,81	B	23,2
Transect 3 (Cast.)	314	-0,71	-5,30	B	25,9
Transect 3 (Cast.)	314	-0,80	-10,09	C3	25,9

Transect 3 (Cast.)	314	-0,49	-9,90	C3	25,9
Transect 3 (Cast.)	314	-0,47	-10,29	C3	25,9
Transect 3 (Cast.)	314	-0,40	-9,97	C3	25,9
Transect 3 (Cast.)	314	0,06	-10,30	C3	25,9
Transect 3 (Cast.)	316	-1,24	-5,50	B	29,2
Transect 3 (Cast.)	316	-1,00	-5,48	B	29,2
Transect 3 (Cast.)	316	-0,22	-4,79	B	29,2
Transect 3 (Cast.)	316	-1,02	-10,21	C3	29,2
Transect 3 (Cast.)	316	-0,18	-9,31	C3	29,2
Transect 3 (Cast.)	316	0,30	-10,37	C3	29,2
Transect 3 (Cast.)	318	-0,28	-4,53	B	35,4
Transect 3 (Cast.)	320	-0,68	-5,79	B	96,1
Transect 3 (Cast.)	322	-0,88	-6,07	B	158,0
Transect 3 (Cast.)	323	-0,65	-5,37	B	188,0
Castellas (ZF1)	Z1,1	0,17	-5,26	C1	0,0
Castellas (ZF1)	Z1,1	0,39	-5,23	C1	0,0
Castellas (ZF1)	Z1,1	0,46	-4,70	C1	0,0
Castellas (ZF1)	Z1,2	0,21	-5,98	C1	0,0
Castellas (ZF1)	Z1,1	-0,55	-6,40	C4	0,0
Castellas (ZF1)	Z1,1	-0,52	-6,10	C4	0,0
Castellas (ZF1)	Z1,2	-4,12	-7,45	C5	0,0
Castellas (ZF1)	Z1,2	-0,15	-4,99	FR	0,0
Castellas (ZF1)	Z1,2	0,39	-4,73	M	0,0
Castellas (ZF1)	Z1,2	0,61	-5,77	M	0,0
Castellas (ZF1)	Z1,1	0,78	-6,16	M	0,0
Castellas (ZF2)	Z2,2	0,77	-5,38	C1	0,0
Castellas (ZF2)	Z2,7	-1,40	-9,52	C3	0,0
Castellas (ZF2)	Z2,7	-4,38	-7,15	C5	0,0
Castellas (ZF2)	Z2,7	-3,97	-7,13	C5	0,0
Castellas (ZF2)	Z2,7	-3,78	-8,04	C5	0,0
Castellas (ZF2)	Z2,7	-3,56	-7,86	C5	0,0
Castellas (ZF2)	Z2,7	-3,24	-7,48	C5	0,0
Castellas (ZF2)	Z2,7	-3,23	-8,54	C5	0,0
Castellas (ZF2)	Z2,2	0,58	-5,47	FR	0,0
Castellas (ZF2)	Z2,2	0,92	-4,91	FR	0,0
Castellas (ZF2)	Z2,7	-1,68	-5,63	FR	0,0
Castellas (ZF2)	Z2,7	-2,24	-6,55	FR	0,0
Castellas (ZF2)	Z2,7	-3,18	-7,38	M	0,0
Castellas (ZF2)	Z2,7	-2,86	-6,03	FR	1,0
Castellas (ZF5)	Z5,4	0,27	-8,25	C3	0,0
Castellas (ZF5)	Z5,4	0,31	-7,87	C3	0,0
Castellas (ZF5)	Z5,4	0,32	-8,23	C3	0,0
Castellas (ZF5)	Z5,4	1,06	-6,34	C1	0,4

Castellas (ZF5)	Z5,4	1,08	-6,76	C1	0,4
Castellas (ZF5)	Z5,4	1,05	-7,13	FR	0,4
Castellas (ZF5)	Z5,4	1,37	-6,03	FR	0,4
Castellas (ZF5)	Z5,4	1,42	-6,15	FR	0,4

Transect	**Sample**	**$\delta^{13}C$ (‰VPDB)**	**$\delta^{18}O$ (‰VPDB)**	**Class**	**Distance to F1 (m)**
Transect 4 (D19)	3B	-0,81	-6,52	B	0,0
Transect 4 (D19)	3B	-1,20	-6,50	C1	0,0
Transect 4 (D19)	3B	-1,02	-6,33	C1	0,0
Transect 4 (D19)	3B	0,11	-6,25	C1	0,0
Transect 4 (D19)	3B	-0,74	-6,23	M	0,0
Transect 4 (D19)	9	-2,32	-7,30	B	9,2
Transect 4 (D19)	13a	-3,44	-8,11	B	14,3
Transect 4 (D19)	13a	-2,96	-7,93	B	14,3
Transect 4 (D19)	13C	-2,97	-7,62	M	14,3
Transect 4 (D19)	13C	-2,86	-7,79	M	14,3
Transect 4 (D19)	13C	-2,70	-8,12	M	14,3
Transect 4 (D19)	13C	-2,67	-7,96	M	14,3
Transect 4 (D19)	13C	-2,66	-8,16	M	14,3
Transect 4 (D19)	13C	-2,50	-7,77	M	14,3
Transect 4 (D19)	13C	-1,54	-8,98	M	14,3
Transect 4 (D19)	17	-2,58	-7,68	B	18,7
Transect 4 (D19)	14A	-1,97	-6,38	B	18,7
Transect 4 (D19)	14A	-1,87	-6,74	B	18,7
Transect 4 (D19)	15B	-2,23	-7,43	B	18,7
Transect 4 (D19)	17	-1,05	-6,40	C1	18,7
Transect 4 (D19)	14A	-1,77	-6,74	C1	18,7
Transect 4 (D19)	14A	-2,42	-6,43	C4	18,7
Transect 4 (D19)	14A	-2,06	-6,67	C4	18,7
Transect 4 (D19)	21	-2,23	-6,54	B	24,4
Transect 4 (D19)	RSG	-1,90	-7,66	B	28,4
Transect 4 (D19)	RSG	-1,70	-7,83	B	28,4
Transect 4 (D19)	RSD	-2,87	-7,10	B	29,5
Transect 4 (D19)	RSD	-2,76	-7,14	B	29,5
Transect 4 (D19)	RSD	-0,93	-9,40	C3	29,5
Transect 4 (D19)	RSF1	-2,40	-7,28	B	34,7
Transect 4 (D19)	RSF2	-2,14	-7,39	B	34,7
Transect 4 (D19)	RSF2	-1,78	-7,27	B	34,7
Transect 4 (D19)	RSF1	-1,03	-9,44	C3	34,7
Transect 4 (D19)	RSF2	-1,93	-8,05	C3	34,7
Transect 4 (D19)	RSF2	-0,59	-9,40	C3	34,7

Transect 4 (D19)	RSF2	-2,95	-8,14	C4	34,7
Transect 4 (D19)	RSE 1	-2,53	-7,33	B	35,0
Transect 4 (D19)	RSE 2	-2,59	-7,41	B	35,0
Transect 4 (D19)	RSE 1	-1,71	-7,68	C3	35,0
Transect 4 (D19)	RSE 2	-1,84	-6,73	C3	35,0
Transect 4 (D19)	57	-2,07	-5,93	B	38,1
Transect 4 (D19)	57	-1,94	-5,87	B	38,1
Transect 4 (D19)	57	-1,83	-7,06	C3	38,1
Transect 4 (D19)	57	-1,10	-6,75	C3	38,1
Transect 4 (D19)	57	-4,02	-7,04	C4	38,1
Transect 4 (D19)	57	-2,17	-5,72	C4	38,1
Transect 4 (D19)	57	-1,58	-6,52	FR	38,1
Transect 4 (D19)	57	-7,20	-5,68	M	38,1
Transect 4 (D19)	57	-7,13	-5,90	M	38,1
Transect 4 (D19)	28b	-1,03	-7,21	B	39,3
Transect 4 (D19)	28b	-1,03	-6,10	C3	39,3
Transect 4 (D19)	28b	-4,09	-6,92	C4	39,3
Transect 4 (D19)	28b	-2,58	-7,40	C4	39,3
Transect 4 (D19)	28b	-2,47	-7,54	C4	39,3
Transect 4 (D19)	30a	-1,61	-7,04	B	42,6
Transect 4 (D19)	30a	-1,41	-6,87	B	42,6
Transect 4 (D19)	30a	-3,23	-7,03	C4	42,6
Transect 4 (D19)	30a	-2,89	-7,45	C4	42,6
Transect 4 (D19)	24a	-1,21	-7,52	B	51,1
Transect 4 (D19)	27b	-1,92	-7,48	B	57,9
Transect 4 (D19)	31	-1,24	-6,44	B	65,0
Transect 4 (D19)	32	-1,75	-7,50	B	67,4
Transect 4 (D19)	34	-1,79	-7,49	B	72,2
Transect 4 (D19)	36	-1,32	-7,21	B	77,8
Transect 4 (D19)	38	-1,73	-7,59	B	81,5
Transect 4 (D19)	62	-1,96	-7,56	B	86,0
Transect 4 (D19)	42	-0,81	-6,80	B	91,9
Transect 4 (D19)	63	-0,55	-5,50	B	124,0
Transect 4 (D19)	64	-1,17	-5,88	B	160,0
Transect 4 (D19)	65	-1,10	-6,57	B	197,0
Transect 4 (D19)	66	-1,31	-5,21	B	236,0
Transect 4 (D19)	60a	-3,06	-9,18	B	255,2
Transect 4 (D19)	60B	-4,80	-8,47	B	255,2
Transect 4 (D19)	60B	-4,66	-8,92	B	255,2
Transect 4 (D19)	61	-1,53	-9,87	C3	255,2
Transect 4 (D19)	61	-1,36	-9,89	C3	255,2
Transect 4 (D19)	60a	-1,15	-9,70	C3	255,2

Transect 4 (D19)	60a	-3,32	-9,11	C4	255,2
Transect 4 (D19)	60B	-5,10	-9,09	C4	255,2
Transect 4 (D19)	60B	-4,73	-8,84	C4	255,2
Transect 4 (D19)	60B	-4,15	-9,18	C4	255,2
Transect 4 (D19)	60B	-4,07	-9,16	C4	255,2
Transect 4 (D19)	60B	-2,90	-9,06	C4	255,2
Transect 4 (D19)	60a	-3,83	-7,85	M	255,2
Transect 4 (D19)	60B	-5,04	-9,17	M	255,2
Transect 4 (D19)	60B	-4,25	-8,14	M	255,2
Transect 4 (D19)	60B	-3,61	-8,58	M	255,2
Transect 4 (D19)	60B	-3,61	-8,13	M	255,2

6. DISCUSSION

1. DIAGENETIC EVOLUTION OF THE FAULT ZONES

The chronological relations between cements can be established via cross-cutting relations and inclusion principles. Indeed, the veins filled with C2 cement cross-cut C1a and C1b cements (Fig. 5B). Thus, C2 cementation post-dated C1 cement. C3 veins cross-cut the C2 veins, but are included within FR1 clasts (Fig. 5B). Hence, C3 cement is prior to FR1 development but is subsequent to C2 cementation. The fault rock 1 (FR1) is related to the first extensional fault activity, consequently, C1, C2 and C3 cementation phases occurred prior to the proper fault plane and

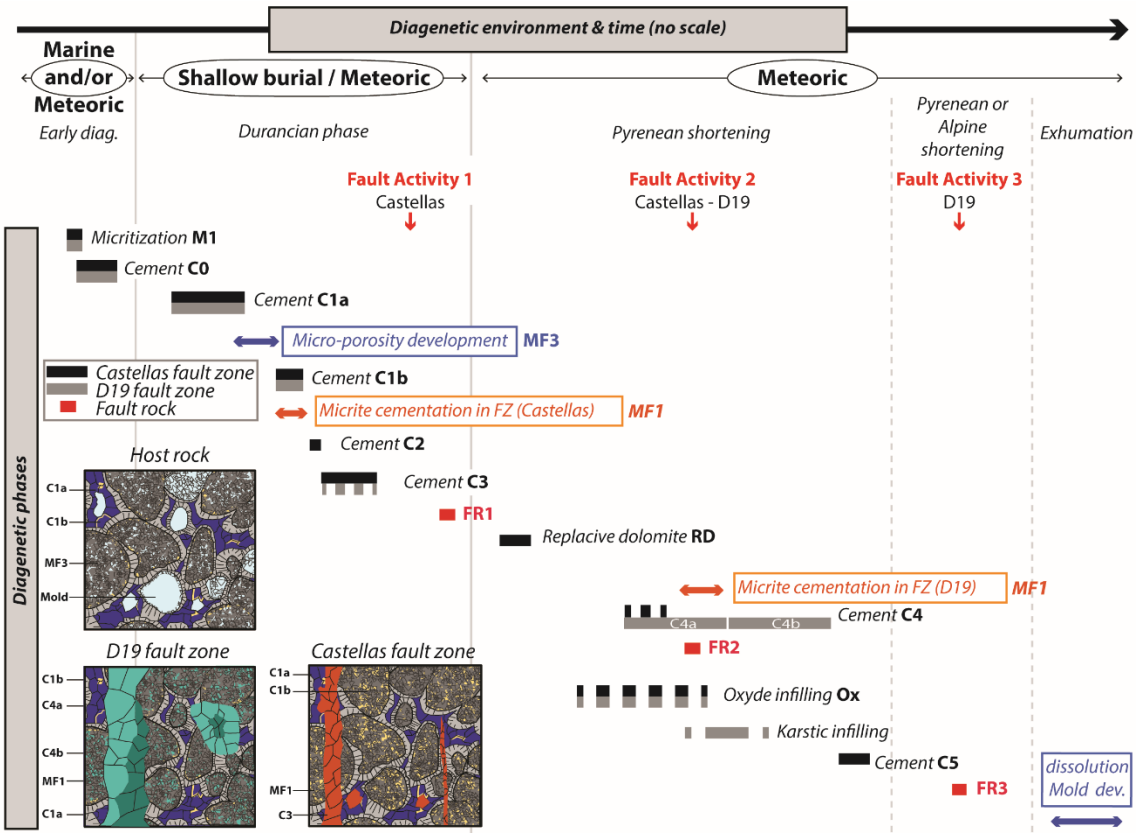

***Figure 7**: Paragenetic sequence of the both fault zones (black: Castellas, grey: D19) with micro-porosity development (blue), cementation (orange) and fault zone activation events (red).*

fault core formation and are related to the fault nucleation. Replacive dolomite is found within FR1 matrix (Fig. 5E), therefore, it developed after FR1 formation. Finally, the C4 cement can be noticed within FR2 matrix indicating that C4 cementation event post-dated FR2 formation. The fault rock 2 (FR2) developed during strike-slip reactivation of the studied faults. The combined superposition, overlap, cross-cutting principles and isotopic signature of cements brought out the chronology between phases, and revealed the paragenetic sequence (Fig. 7).

The Urgonian carbonates in La Fare anticline underwent 3 major diagenetic events, which impacted the host rock and/or the fault zones. We discriminate among diagenetic events that occurred before and during faulting.

a. Pre fault diagenesis – microporosity development

During Upper Barremian, just after deposition, micro-bores organisms at the sediment-water interface enhanced the formation of micritic calcitic envelopes on bioclasts, ooids and peloids (Purser, 1980; Reid and Macintyre, 2000; Samankassou et al., 2005; Vincent et al., 2007). This micritisation in marine conditions is typical for Urgonian low-energy inner platform environment (Fournier et al., 2011; Masse, 1976). Subsequently, C0 cement formed around grains giving rise to a solid envelop inducing the preservation of the original grain shape during the later burial compaction (Step 0 on Fig. 8). However, the majority of isotopic values does not fit in the Barremian sea water calcite box which ranges from -4.00‰ to -1.00‰ for $\delta^{18}O$ and from +1.00‰ to +3.00‰ for $\delta^{13}C$ (Fouke et al., 1996; Godet et al., 2006). Only two data points pertaining to micritised grains show isotopic values close the Barremian sea water calcite. The isotopic depletion of other data indicates the slight impact of C0 cementation on isotopic values.

The next sub-phase of cementation C1a partly fills intergranular porosity. This non luminescent cement with isotopic values ranging from -6.8‰ to -3.9‰ for $\delta^{18}O$ and from -1.0‰ to +1.3‰ for $\delta^{13}C$ is characteristic of mixed fluids. Léonide et al. (2014) measured a calcite cement S1, near La Fare anticline with similar luminescence and isotopic range values (mean: $\delta^{18}O$= −5.49‰; $\delta^{13}C$=+2.34‰). These authors linked this cementation phase to a shallow burial meteoric fluid circulation under equatorial climate during Durancian uplift. This diagenetic event led to micrite re-crystallization, and to the development of microporosity (MF3). Since La Fare carbonates were exhumed at that time (Léonide et al., 2014) the meteoric fluids led to similar diagenetic modifications (Step 1 on Fig. 8):

(i) Micrite re-crystallization and microporosity MF3 setup by Ostwald ripening processes (Fig. 9B1a; Ostwald, 1886; Volery et al., 2010).
(ii) Cementation of C1a, partly filling intergranular porosity (Fig. 9B1b)

The micrite re-crystallization strongly increased rock porosity due to enhanced microporosity (Fig. 9B1a). Resulting from this event, Urgonian carbonates formed a type III reservoir *sensu* Nelson (2001).

b. Fault-related diagenesis – alteration of reservoir properties

Normal faulting-related diagenesis

The Castellas fault first nucleated during Durancian uplift (Aubert et al., 2019b; Matonti et al., 2012) affecting the host Urgonian carbonates.

In porous granular media, fault nucleation mechanisms can lead to dilation processes (Fossen and Bale, 2007; Fossen and Rotevatn, 2016; Main et al., 2000; Wilkins et al., 2007; Zhu and Wong, 1997) under low-confining pressure (<100 KPa; Alikarami and Torabi 2015). Because this process leads to dilatancy, it increases the rock permeability (Alikarami and Torabi, 2015; Bernard et al., 2002) in the first stage of deformation bands development (Heiland et al., 2001; Lothe et al., 2002) enhancing fluid flows.

Castellas fault zone nucleated within a partially and dimly cemented host rock under low-confining pressure, in an extensional stress regime, at a depth <1 km (Lamarche et al. 2012). Under these conditions, Barremian host rocks were likely characterised by mechanical and petrophysical properties close to porous granular media described above. Moreover, Micarelli et al. (2006) showed that, during early stages of deformation, fault zones in carbonates have a hydraulic behaviour comparable to deformation bands in carbonates. Hence, in the Urgonian carbonates of La Fare area, dilatant processes occurred as an incipient fault mechanism and enhanced fluid circulations along the deformation bands. Fluid flows led to the cementation of C1b (Step 2 on Fig. 8). However, dilation bands were likely unstable and grain collapse occured swiftly after the beginning of the deformation due to an increase in the loading stress (Lothe et al., 2002). This could explain why C1b does not fill all intergranular porosity. Consequently, as all micritic grains in fault zone are cemented by C1b, the bulk isotopic measurements are strongly influenced by C1 cement isotopic values. This is the explanation why in transect 3 the bulk isotopic values 30 m apart from the fault (means of -5.26‰ for $\delta^{18}O$ and -0.82‰ for $\delta^{13}C$) are close to bulk isotopic values far from the fault plane (188 m; -5.37‰ for $\delta^{18}O$ and -0.65‰ for $\delta^{13}C$, Fig. 6A). Dilation bands have also been described by *Kaminskaite et al.* (2019) in the San Vito Lo Capo carbonates grainstones (Sicily, Italy). These dilation bands also led to selective cementation of the carbonate rocks and to a microporosity decrease.

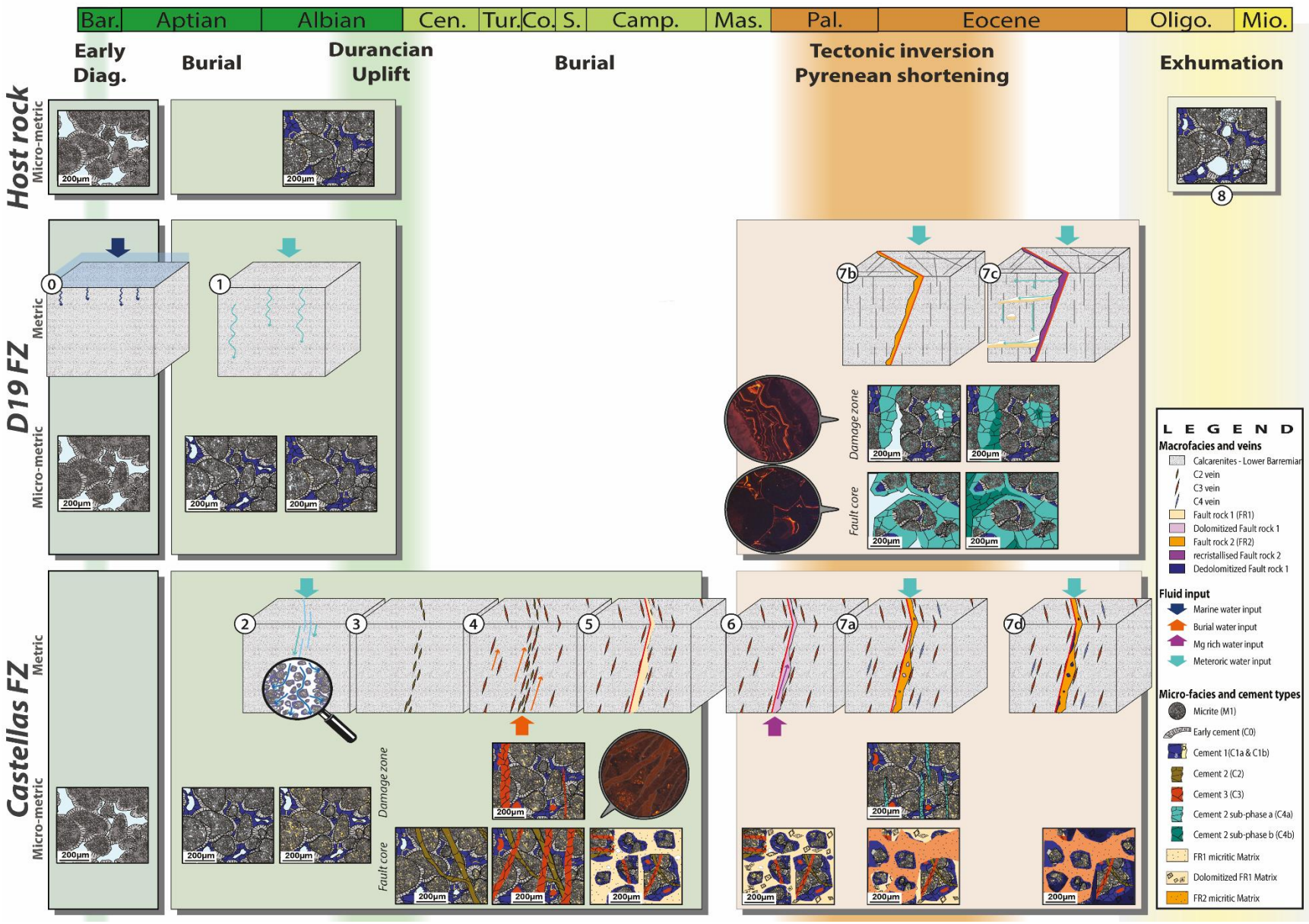
Bar.
Aptian
Albian
Cen.
Tur.
Co.
S.
Camp.
Mas.
Pal.
Eocene
Oligo.
Mio.
Early Diag.
Burial
Durancian Uplift
Burial
Tectonic inversion Pyrenean shortening
Exhumation
Host rock
Micro-metric
D19 FZ
Metric
Micro-metric
Castellas FZ
Metric
Micro-metric
Damage zone
Fault core
200µm
0
1
2
3
4
5
6
7a
7b
7c
7d
8
LEGEND
Macrofacies and veins
Calcarenites - Lower Barremian
C2 vein
C3 vein
C4 vein
Fault rock 1 (FR1)
Dolomitized Fault rock 1
Fault rock 2 (FR2)
recristallised Fault rock 2
Dedolomitized Fault rock 1
Fluid input
Marine water input
Burial water input
Mg rich water input
Meteroric water input
Micro-facies and cement types
Micrite (M1)
Early cement (C0)
Cement 1(C1a & C1b)
Cement 2 (C2)
Cement 3 (C3)
Cement 2 sub-phase a (C4a)
Cement 2 sub-phase b (C4b)
FR1 micritic Matrix
Dolomitized FR1 Matrix
FR2 micritic Matrix

Figure 8 *: Diagenetic and geodynamic evolution since the Barremian of both fault zones and host rock at the metric and micro-metric scale. Numbers 0 to 8 correspond to the steps 0 to 8 (see text for description).*

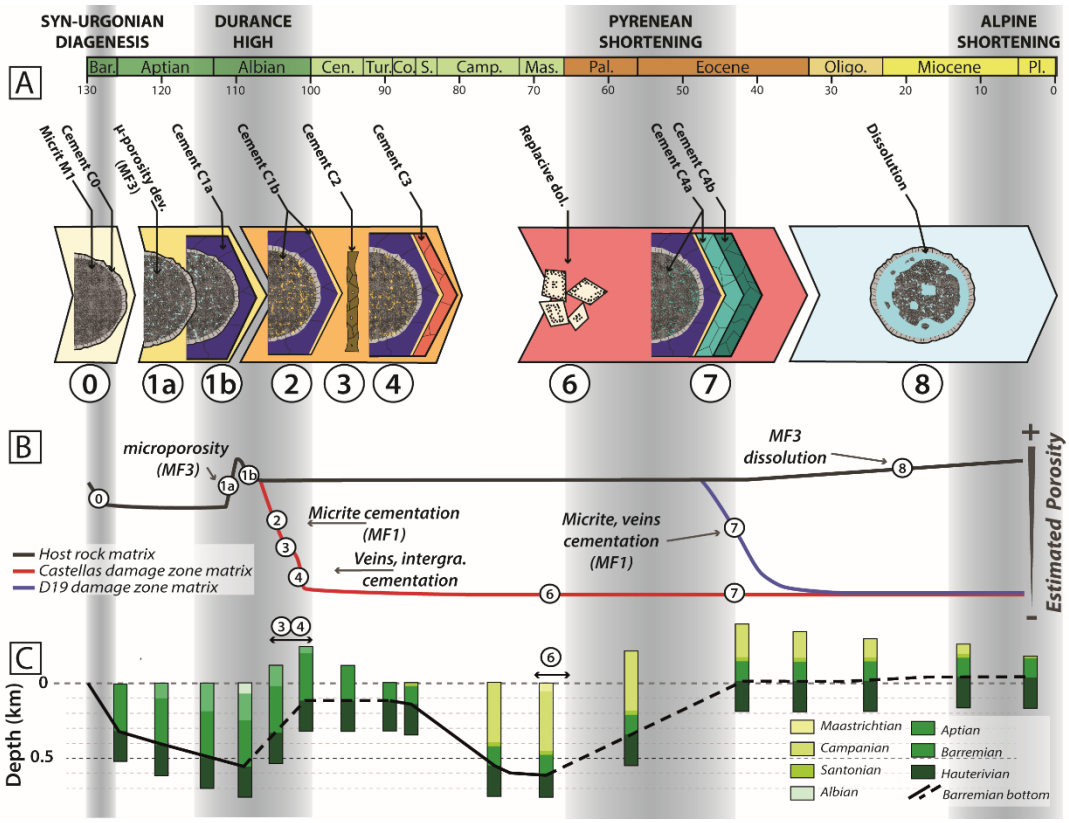

Figure 9 *: Evolution of reservoir properties. A: different cementation phases; numbers 0 to 8 correspond to the steps 0 to 8 (see text for description), B: relative porosity evolution of the host rock and the two fault zones; C: Burial/Uplift curve of Barremian basement (modified from Matonti et al. (2012)).*

Cementation (C1a and C1b) conferred a stiffer response of limestone to deformation, making it prone to deform through brittle structures (joints and veins), rather than via granular particulate flow (deformation bands). During the first stages of fault evolution in low-porosity limestones, intense fracturing of the fault zone predating fault core formation is known to increase fault permeability (Micarelli et al., 2006). In the studied faults, the first brittle event allowed Al-rich fluids to flow with fine-grained quartz grains in the incipient open fractures leading to precipitation of C2 cement (Step 3 on Fig. 8). The Urgonian facies of the studied area are composed of pure carbonates without siliciclastic input. Quartz grains and Aluminium could have been reworked from surrounding formations. The rocks underlying the studied exposed Urgonian carbonates are limestones and dolostones. Albian and Aptian rocks are marly and sandy limestones, respectively (Anglada et al., 1977). Hence, Aptian layers are very likely to be the source of quartz. The fluids may have carried small grains of quartz from the Aptian sandy limestones via the fracture network. The Al enrichment of C2 could result from the erosion of Albian and Aptian deposits during the Durancian uplift (Guendon and Parron, 1985; Triat, 1982).

As the fault zone grew, new fracture sets formed, leading to new phase of calcite cementation (C3) in veins and intergranular porosity (Step 4 on Fig. 8). The $\delta^{18}O$ isotopic values of C3 range from -

10.40‰ to -6.73‰ with $\delta^{13}C$ values between -2.09‰ and +1.22‰. As C3 cementation occurred during the Durancian uplift and denudation, it most probably did not cement in deep burial conditions (maximum depth of 500 m; Fig. 9C4). The negative $\delta^{13}C$ values tend corroborate the hypothesis of cementation induced by meteoric fluids rather than marine ones. Hence, C3 would correspond to a shallow burial/meteoric cementation phase. Due to this cementation, rocks in this zone tightened with porosity down to <5%. The porosity did not change since this event (Fig. 9B5). This porosity reduction due to cementation has also been observed in other cases of brittle-dilatant faults (Agosta et al., 2007; Celico et al., 2006; Gaviglio et al., 2009; Mozley and Goodwin, 1995). Following this, the fault zone was a barrier to fluid flow, leading to a reservoir compartmentalization. Fluids responsible for precipitation of C3 cement also occurred along fracture clusters of the D19 sector and led to vein formation.

In a later stage, the fault core formed and the fault plane *sensu-stricto* developed, leading to FR1 breccia with a permeable matrix with quartz grains >100 µm in size (Step 5 on Fig. 8). These grains either came from silica found inside C2 cement described above or from Aptian overlying rocks. Silica crystals in C2 veins are scarce and smaller than 10 µm. Thus, quartz grains may rather come from Aptian rocks like the ones found in C2 veins. The presence of Aptian quartz in the fault core proves that the Castellas fault affected also Aptian rocks, which were later eroded during the Durancian uplift. According to this, the fault activity occurred before total erosion of Aptian rocks. Un-cemented breccias within the fault core formed good fluid pathways (Billi et al., 2008; Delle Piane et al., 2016). In the studied fault, formation of FR1 breccia allowed the fault core to act as a drain. However, the cemented surrounding host rocks constrained the lateral extent of the drainage area of this high-permeable conduit. Un-cemented breccias acting as good across- and along- fluid pathways were also described on Apennine carbonate formations within fault cores of strike-slip and extensional faults (Billi et al., 2003, 2008; Storti et al., 2003).

Tectonic Inversion – Castellas fault-related dolomitization

At the onset of the Pyrenean shortening, compressive stresses led to underground water upwelling through the permeable fault core. This fluid flow triggered the dolomitization of FR1 matrix (Step 6 on Fig. 8). This matrix-selective dolomitization could have been favoured by several factors:

(i) The matrix has higher permeability than cemented clasts with a smaller grain size, hence a higher grain surface area (Machel, 2004);

(ii) This type of upwelling fluids, so-called “squeegee-type”, are short-lived processes (Buschkuehle and Machel, 2002; Deming et al., 1990; Dorobek, 1989; Machel et al., 2000) not favourable for massive dolomitization;

(iii) Low-temperature fluids, under 50°-80°C, enabled the preservation of FR1 clast initial structure. Contrarily, high-temperature dolomitization tends to be destructive (Machel, 2004);

(iv) The tight surrounding host rock constrained Mg-rich fluid circulation to the fault core domain.

Gisquet et al. (2013) noticed similar fault-related replacive dolomitization phase in the Etoile massif, 23 km South-Est of the studied zones. They linked the dolomitization to contractional stress regime during the early (Late Cretaceous) Pyrenean shortening. According to these authors, the tectonic stress led to low-temperature upwelling fluids likely Mg-enriched by the dissolution of underlying Jurassic dolomites. The Jurassic dolomites also occur in La Fare anticline. Since the fluids leading to dolomitization of fault core were low-temperature and since dolomites occur underground, it is possible that the dolomitization in La Fare and in the Etoile massif were similar and synchronous. Matrix dolomitization can increase inter-crystalline and/or inter-particle porosity up to 13% but the later dolomite overgrowth reduces the porosity and permeability (Lucia, 2004; Machel, 2004; Saller and Henderson, 2001). Hence, in the first stages of dolomitization, the fault core was an important drain. After the growth of dolomite crystals, the fault core turned into barrier (Fig. 9 B6 and C6)

Sinistral tectonic inversion – meteoric alteration of reservoir properties

The ongoing tectonic inversion with increasing compressive stresses eventually led to the Castellas fault sinistral reactivation and to the onset of D19 fault zone (Aubert et al., 2019b). Aubert et al. (2019a) has shown that this compression reactivated the pre-existing early N030° background fractures (Step 7 on Fig. 8). This tectonic event formed FR2 in fault cores but with specific diagenetic consequences. In the D19 fault zone, the fault nucleation and reactivation of background fractures led to pluri-metric to kilometric fault surfaces with a permeable fault rock acting as drains and localizing the fluid flow (Aubert et al., 2019a). This fluid flow witnessed by the cementation of C4a and C4b in veins and micritised grains (MF1, Step 7c on Fig. 8), led to a strong porosity decrease in the fault zone (Fig. 9, B7 and C7). However, not all fractures were cemented by C4, so that fracture porosity/permeability was still partially preserved. Therefore, the D19 fault zone became a type I reservoir *sensu* Nelson (2001) with a very low matrix porosity/permeability and high fracture-related secondary permeability (Aubert et al., 2019a).

Along F2, successive fluids gave rise to karsts, karstic infilling and dissolution/cementation processes of FR2 matrix (Step 7c on Fig. 8). Then, FR2 was sealed by C4 cementation. Isotopic values of C4 cement (from -9.2 to -6.1‰ for $\delta^{18}O$ and from -5.01‰ to -1.0‰ for $\delta^{13}C$) highlight the strong influence of meteoric fluids. This is coherent with the occurrence of karstic infilling due to fluid circulations in vadose zone, with alternating dissolution and cementation (Swart, 2015). However, the positive covariance between $\delta^{18}O$ and $\delta^{13}C$ of C4 suggests mixed fluids (Allan and Matthews, 1982) of meteoric water and burial or marine water.

In the Castellas fault zone, the host rocks are slightly impacted by these meteoric fluid circulations. Yet, some veins filled with C4a cement occur along transect 2 and 3 (Step 7a on Fig. 8). Two samples have enriched $\delta^{18}O$ and $\delta^{13}C$ isotopic values (respective means of -6.25‰ and -4.20‰ for $\delta^{18}O$; -0.64 and -0.09‰ for $\delta^{13}C$) similar to C1 cement (Fig. 6A). This indicates that C4 cement in the Castellas fault zone was precocious in comparison to the D19. C4 cement in Castellas area is restricted to transect 2. Transect 2 cross-cuts the Castellas fault along a relay zone (Fig. 2A). Relay or linkage zones occur where two fault segments overlap each other during fault grow (Kim et al., 2004; Long and Imber, 2011; Walsh et al., 1999, 2003). Consequently, the fault complexity, the fracture intensity and the fracture-strike range are increased (Kim et al., 2004; Sibson, 1996). This

process in the studied area resulted in a well-connected fracture network that increased the permeability and favoured local fluid circulations. In transect 2, the increase of the local permeability in the relay zone enhanced fluid flow related to C4 cement. The relay zones along the Castellas fault and their consequences on the fracture permeability are, therefore, responsible for this local cementation event. On the contrary, cementation in D19 fault zone is linked to the highly permeable fault surfaces which acted as drains (Aubert et al., 2019a). This implies that the cementation occurred only after the development of the fault surface. In the case of Castellas, the relay zone was already present, inherited from the former extensional activity, allowing early C4 fluid to flow through the fault zone. This, in addition, explains why the early C4 cementation has not been recorded in D19 fault zone. The C4 cementation in transect 2 reduced porosity to less than 8% on a wider zone (>60 m) than in both other transects (transect 1 ≈30 m, transect 3>40 m).

The reactivation of the Castellas fault formed a new fracture network that locally triggered the fracture connectivity and permeability. The Castellas fault zone formed a type I reservoir (Nelson, 2001), but lateral variation of the fracture network implies lateral variations of the hydraulic properties. Thus, the fault zone was both a drain and a barrier (Matonti et al., 2012). In this case, the most appropriate concept would be a sieve, because in this analogy, it is synchronously closed in places and open in other places.

After these events, the matrix of the Castellas fault core was de-dolomitized (FR1) in relation to cementation C5 (Step 7d on Fig. 8). The C5 cement isotope values (mean of -7.49‰ for $\delta^{18}O$ and -4.01‰ for $\delta^{13}C$) are comprised within C4 positive covariance between $\delta^{18}O$ and $\delta^{13}C$. This indicates a continuity between C4 and C5 fluid flows. The measurements with the SEM revealed a lack of Mg in the matrix indicating that C5 totally recrystallised the replacive dolomite. Following this de-dolomitization phase, no additional diagenetic event is recorded in Castellas fault zone.

A late Pyrenean to Alpine compression reactivated the D19 fault zone that formed the new fault rock FR3. The matrix of this fault rock has very low $\delta^{13}C$ isotopic values (mean of -6.83‰) indicating an organic matter input (Swart, 2015). This implies fluids percolating soils, as results from a near surface fluid circulation. We deduce that the D19 faults was lately reactivated after the folding of the La Fare anticline. There is no such cementation with similar isotope values in the fault zone, meaning that fluids and cements did not alter the fault zone diagenetic properties.

Eventually, the late exhumation of the Urgonian carbonate host rocks led to flows inducing dissolution of MF3 grains in the host rock. This phase produced the moldic porosity and increased the porosity/permeability (Step 8 on Fig. 9B and C). These fluids, however, did not affect fault zones.

2. EVOLUTION OF FAULT ZONES RESERVOIR PROPERTIES

The host rock presents a monophasic evolution and switch from a type IV reservoir where matrix provided storage and flow, to a type III reservoir where fractures behave as pathways towards fluid flow but the production mainly comes from the matrix (*Nelson* 2001, Fig. 10A). The fault zones present a more complex polyphasic evolution than the host rock. Indeed, their reservoir properties evolved from a type IV reservoir corresponding to the host rock to a type I reservoir where fractures provide both storage and flow pathways (*Nelson* 2001, Fig. 10A). Both fault zones present slight

differences. The Castellas fault zone was completely tight soon after C3 cementation. Consequently, it did not fit to the Nelson reservoir type classification. However, after fault core formation, the fault zone presents a high fault core permeability. In this study we propose a new approach with a triangle diagram taking into account fault core permeability to remove the flaws of this method (Fig. 10B). The percentage assigned to the fault core or to the matrix are qualitatively estimated. Further quantification could be evaluated, for instance, with the width of the fault core and damage zone domains, or by estimating the fracture network volume. However, no recent study have provided such quantification. Thus, for Castellas fault zone, permeability evolves from a stage with exclusive contribution from the host rock permeability (100% matrix; step 0 on Fig. 10B) to a permeability due to 50% to the

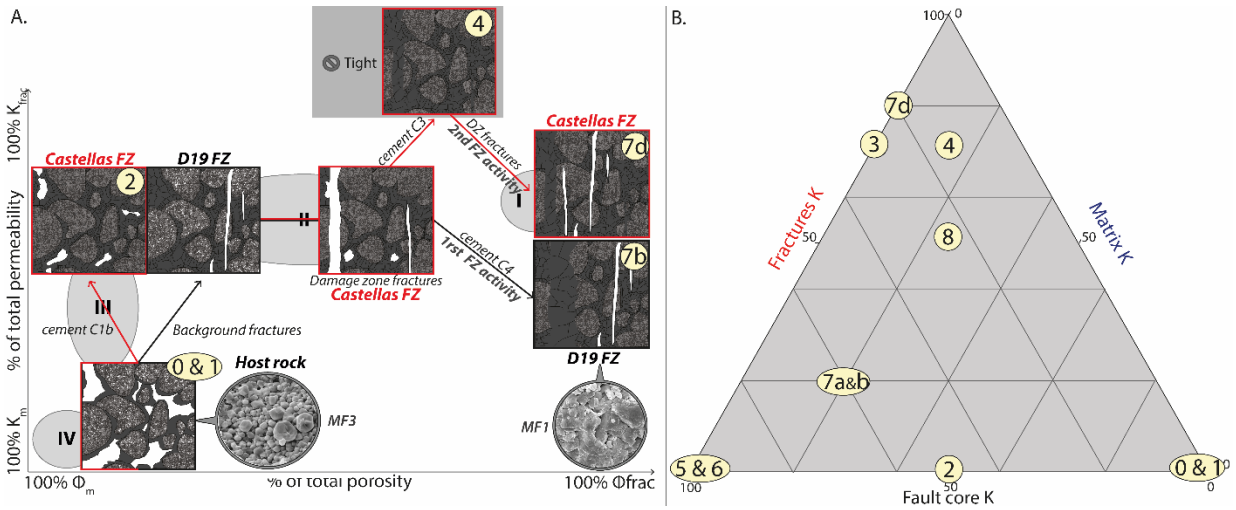

Figure 10 *: Castellas and D19 fault zone reservoir properties evolution. A: evolution of permeability and porosity taking into account fault zone fractures and matrix after Nelson (2001) and B: Triangle diagram of permeability evolution with 3 components: matrix, fractures and fault core. Numbers 1 to 8 correspond to the steps 1 to 8 (see text for description). K: Permeability, Φ: Porosity, FZ: Fault Zone, DZ: Damage Zone, MF1 and MF3: Micrite micro-fabric.*

matrix and 50% to the fault core during dilation band development (step 2 on Fig. 10B). Thereafter, during the two fracture events permeability is mainly linked to fracturing (C2: 30% fault core, 70% fractures; C3: 15% fault core, 15% matrix, 70% fractures; step 3, 4 on Fig. 10B). Then, after fault core formation and during dolomitization event, permeability is solely provided by the fault core (step 6, 7 on Fig. 10B). Lastly, after fault zone reactivation, the permeability is due to 20% to the fault core and 80% to fractures (step 7c on Fig. 10B). The D19 fault zone permeability during its development was related for 20% to the matrix, 20% to the fractures and 60% to the fault core (step 7a and 7b on Fig. 10B).

8. CONCLUSION

This study deciphered the diagenetic evolution of two fault zones and the impact on reservoir properties of both faults and host rock in the frame of the overall geodynamic context of the SE Basin. The main outcomes are:

- Fault zones may have a complex diagenetic history, but most diagenetic phases occur during the nucleation of the fault. In the case of Castellas fault zone, the diagenetic imprint

is mainly influenced by early diagenesis occurring along fractures and diffuse dilation zones prior to the proper fault plane nucleation. Regarding D19 fault zone, most of diagenetic alterations occurred just after fault onset in the first stage of its activity. In both cases, the cementation altered initial reservoir properties in the fault zone vicinity, switching from type III to type I during the first stages of fault development. Later fault reactivation slightly impacts matrix porosity/permeability.

- Fault zones act as drains canalizing fluid flows in the beginning of their development. This induces fault zone cementation but preservation of host rock microporosity. This important fluid drainage is visible on D19 outcrop where the flowing fluids led to dissolution/cementation of fault rock matrix and formed karsts.
- All diagenetic stages, including cementation and dolomitization, result from low-temperature fluids with important meteoric water input. These low-temperature fluid flows associated with the deformation and cementation types, and, the lack of mineralisation specific to high-temperature fluids disprove any significant hydrothermal influence.

This regional study allows to draw broader rules for complex faults with polyphasic activity affecting granular carbonates at shallow burial conditions (Fig. 9).

- Under extensional context, fault nucleation can lead to the development of dilation bands acting as conduits for fluid flow. Carbonates are very sensitive to rock-fluids interactions. Thus, the onset of dilation bands triggers important diagenetic reactions that strongly alter local reservoir properties. During later fault zone development, the diagenesis depends on fault zone internal architecture.
- Fracture networks related to fault nucleation in granular carbonates form good fluid pathways before proper fault plane formation. However, in the case of pre-fractured carbonates, like D19 fault zone, fault rocks early appear in fault cores. In these cases, fluids flowed preferentially within the permeable breccia rather than in the damage zone.

Acknowledgement

We would like to thank Suzan Verdegaal, Lionel Marié and Alain Tonetto for support they provide during this study. We grateful to Editor Kei Ogata, and Fabrizio Agosta, Mattia Pizzati and Eric Salomon who made critical suggestions to improve this paper.

REFERENCES

Agosta, F., Prasad, M. and Aydin, A.: Physical properties of carbonate fault rocks, Fucino Basin (Central Italy): implications for fault seal in platform carbonates, Geofluids, 7, 19–32, doi:10.1111/j.1468-8123.2006.00158.x, 2007.

Agosta, F., Mulch, A., Chamberlain, P. and Aydin, A.: Geochemical traces of CO2-rich fluid flow along normal faults in central Italy, Geophys. J. Int., 174(2), 1074–1096, doi:10.1111/j.1365-246X.2008.03792.x, 2008.

Agosta, F., Alessandroni, M., Antonellini, M., Tondi, E. and Giorgioni, M.: From fractures to flow: A field-based quantitative analysis of an outcropping carbonate reservoir, Tectonophysics, 490(3–4), 197–213, doi:10.1016/j.tecto.2010.05.005, 2010.

Agosta, F., Ruano, P., Rustichelli, A., Tondi, E., Galindo-Zaldívar, J. and Sanz de Galdeano, C.: Inner structure and deformation mechanisms of normal faults in conglomerates and carbonate grainstones (Granada Basin, Betic Cordillera, Spain): Inferences on fault permeability, J. Struct. Geol., 45, 4–20, doi:10.1016/j.jsg.2012.04.003, 2012.

Alikarami, R. and Torabi, A.: Geomechanics for Energy and the Environment Micro-texture and petrophysical properties of dilation and compaction shear bands in sand, Geomech. Energy Environ., 3, 1–10, doi:10.1016/j.gete.2015.06.001, 2015.

Allan, J. R. and Matthews, R. K.: Isotope signatures associated with early meteoric diagenesis, Sedimentology, 29(6), 797–817, doi:10.1111/j.1365-3091.1982.tb00085.x, 1982.

Allmendinger, R. W., Cardozo, N. and Fisher, D. M.: Structural geology algorithms: Vectors and tensors, Cambridge Univ. Press, 9781107012, 1–289, doi:10.1017/CBO9780511920202, 2013.

Anglada, R., Arlhac, P., Catzigras, F., Colomb, E., Damiani, L., Durand, J. P., Durozoy, G., Guieu, G., Masse, J. P., Nury, D., Philip, J., Rouire, J., Rousset, C., Roux, R. M. and Blanc, J. J.: Notice explicative. Carte géologique de la France a 1/50 000. Martigues - Marseille., 1977.

Aubert, I., Lamarche, J. and Léonide, P.: Deciphering background fractures from damage fractures in fault zones and their effect on reservoir properties in microporous carbonates (Urgonian limestones, SE France), Pet. Geosci., doi:DOI10.1144/petgeo2019-010, 2019a.

Aubert, I., Lamarche, J., Richard, P. and Leonide, P.: Imbricated Structure and Hydraulic Path Induced by Strike Slip Reactivation of a Normal Fault in Carbonates, in Fifth International Conference on Fault and Top Seals, p. 4., 2019b.

Bense, V. F., Gleeson, T., Loveless, S. E., Bour, O. and Scibek, J.: Fault zone hydrogeology, Earth-Science Rev., 127, 171–192, doi:10.1016/j.earscirev.2013.09.008, 2013.

Bernard, X. Du, Eichhubl, P. and Aydin, A.: Dilation bands : A new form of localized failure in granular media, 29(24), 1–4, doi:10.1029/2002GL015966, 2002.

Besson, D.: Architecture du bassin rhodano-provençal miocène (Alpes , SE France) : relations entre déformation, physiographie et sédimentation dans un bassin molassique d'avant-pays, Ecole des Mines, Paris., 2005.

Bestani, L.: Géométrie et cinématique de l'avant-pays provençal : Modélisation par coupes équilibrées dans une zone à tectonique polyphasée, Aix-Marseille University, 2015.

Bestani, L., Espurt, N., Lamarche, J., Bellier, O. and Hollender, F.: Reconstruction of the Provence Chain evolution, Southeastern France, Tectonics, 35, 1506–1525, doi:10.1002/2016TC004115, 2016.

Billi, A., Salvini, F. and Storti, F.: The damage zone-fault core transition in carbonate rocks: Implications for fault growth, structure and permeability, J. Struct. Geol., 25(11), 1779–1794, doi:10.1016/S0191-8141(03)00037-3, 2003.

Billi, A., Primavera, P., Soligo, M. and Tuccimei, P.: Minimal mass transfer across dolomitic granular fault cores, Geochemistry, Geophys. Geosystems, 9(1), doi:10.1029/2007GC001752, 2008.

Borgomano, J., Masse, J., Maskiry, S. Al, Borgomano, J. and International, S.: The lower Aptian Shuaiba carbonate outcrops in Jebel Akhdar, northern Oman: Impact on static modeling for Shuaiba petroleum reservoirs, Bull. Am. Assoc. Pet. Geol., 9(9), 1513–1529, doi:10.1306/61EEDCE2-173E-11D7-8645000102C1865D, 2002.

Borgomano, J., Masse, J. P., Fenerci-Masse, M. and Fournier, F.: Petrophysics of lower cretaceous platform carbonate outcrops in provence (SE France): Implications for carbonate reservoir characterisation, J. Pet. Geol., 36(1), 5–41, doi:10.1111/jpg.12540, 2013.

Bruna, P., Guglielmi, Y., Viseur, S., Lamarche, J. and Bildstein, O.: Coupling fracture facies with in-situ permeability measurements to generate stochastic simulations of tight carbonate aquifer properties: Example from the Lower Cretaceous aquifer , Northern Provence , SE France, J. Hydrol., 529, 737–753, doi:10.1016/j.jhydrol.2015.08.054, 2015.

Buschkuehle, B. E. and Machel, H. G.: Diagenesis and paleo fluid flow in the Devonian Southesk-Cairn carbonate complex in Alberta, Canada, Mar. Pet. Geol., 19, 219–227, doi:10.1016/S0264-8172(02)00014-4, 2002.

Caine, J. S., Evans, J. P. and Forster, C. B.: Fault zone architechture and permeability structure, Geology, 24(11), 1025–1028, doi:10.1130/0091-7613(1996)024<1025, 1996.

Cardozo, N. and Allmendinger, N. W.: Sperical projections with OSXStereonets, Comput. Geosci., 51, 193–205,

doi:10.1016/j.cageo.2012.07.021, 2013.
Celico, F., Petrella, E. and Celico, P.: Hydrogeological behaviour of some fault zones in a carbonate aquifer of Southern Italy: An experimentally based model, Terra Nov., 18(5), 308–313, doi:10.1111/j.1365-3121.2006.00694.x, 2006.
Champion, C., Choukroune, P. and Clauzon, G.: La déformation post-miocène en provence occidentale, Geodin. Acta, 13(2–3), 67–85, doi:10.1080/09853111.2000.11105365, 2000.
Chester, F. M. and Logan, J. M.: Implications for Mechanical Properties of Brittle Faults from Observations of the Punchbowl Fault Zone, California, PAGEOPH, 124(1/2), 79, doi:10.1007/BF00875720, 1986.
Chester, F. M. and Logan, J. M.: Composite planar fabric of gouge from the Punchbowl Fault, California, J. Struct. Geol., 9(5–6), doi:10.1016/0191-8141(87)90147-7, 1987.
Delle Piane, C., Giwelli, A., Clennell, M. Ben, Esteban, L., Nogueira Kiewiet, M. C. D., Kiewiet, L., Kager, S. and Raimon, J.: Frictional and hydraulic behaviour of carbonate fault gouge during fault reactivation — An experimental study, Tectonophysics, 690(PartA), 21–34, doi:10.1016/j.tecto.2016.07.011, 2016.
Deming, D., Nunn, A. and Evans, D. G.: Thermal Effects of Compaction-Driven Groundwater Flow, 95(89), 6669–6683, doi:10.1029/JB095iB05p06669, 1990.
Demory, F. R., Conesa, G. I., Oudet, J. U., Mansouri, H. A. and Münch, P. H.: Magnetostratigraphy and paleoenvironments in shallow-water carbonates : The Oligocene- Miocene sediments of the northern margin of the Liguro- Provençal basin (West Marseille , southeastern France), Bull. Soc. géol. Fr., 1, 37–55, doi:10.2113/gssgfbull.182.1.37, 2011.
Deville de Periere, M., Durlet, C., Vennin, E., Lambert, L., Bourillot, R., Caline, B. and Poli, E.: Morphometry of micrite particles in cretaceous microporous limestones of the middle east: Influence on reservoir properties, Mar. Pet. Geol., 28(9), 1727–1750, doi:10.1016/j.marpetgeo.2011.05.002, 2011.
Deville de Periere, M., Durlet, C., Vennin, E., Caline, B., Boichard, R. and Meyer, A.: Influence of a major exposure surface on the development of microporous micritic limestones - Example of the Upper Mishrif Formation (Cenomanian) of the Middle East, Sediment. Geol., 353, 96–113, doi:10.1016/j.sedgeo.2017.03.005, 2017.
Dorobek, S.: migration of erogenic fluids through the Siluro-Devonian Helderberg Group during late Paleozoic deformation: constraints on fluid sources and implications for thermal histories of sedimentary basins presence, , 159, 25–45, doi:10.1016/0040-1951(89)90168-6, 1989.
Eltom, H. A., Gonzalez, L. A., Hasiotis, S. T., Rankey, E. C. and Cantrell, D. L.: Paleogeographic and paleo-oceanographic influences on carbon isotope signatures: Implications for global and regional correlation, Middle-Upper Jurassic of Saudi Arabia, Sediment. Geol., 364, 89–102, doi:10.1016/j.sedgeo.2017.12.011, 2018.
Espurt, N., Hippolyte, J. C., Saillard, M. and Bellier, O.: Geometry and kinematic evolution of a long-living foreland structure inferred from field data and cross section balancing, the Sainte-Victoire System, Provence, France, Tectonics, 31(4), doi:10.1029/2011TC002988, 2012.
Evans, J. P., Forster, C. B. and Goddard, J. V.: Permeability of fault-related rocks, and implications for hydraulic structure of fault zones, J. Struct. Geol., 19(11), 1393–1404, doi:10.1016/S0191-8141(97)00057-6, 1997.
Ferraro, F., Agosta, F., Ukar, E., Grieco, D. S., Cavalcante, F., Belviso, C. and Prosser, G.: Structural diagenesis of carbonate fault rocks exhumed from shallow crustal depths: An example from the central-southern Apennines, Italy, J. Struct. Geol., 122(February), 58–80, doi:10.1016/j.jsg.2019.02.008, 2019.
Florida, S., Maliva, R. G., Missimer, T. M., Clayton, E. A. and Dickson, J. A. D.: Diagenesis and porosity preservation in Eocene microporous limestones , Sediment. Geol., 217(1–4), 85–94, doi:10.1016/j.sedgeo.2009.03.011, 2009.
Ford, M., Duchene, S., Gasquet, D. and Vanderhaeghe, O.: Two-phase orogenic convergence in the external and internal SW Alps, J. Geol. Soc. London., 163(5), 815–826, doi:10.1144/0016-76492005-034, 2006.
Fossen, H. and Bale, A.: Deformation bands and their influence on fluid flow, 12(12), 1685–1700, doi:10.1306/07300706146, 2007.
Fossen, H. and Rotevatn, A.Fault linkage and relay structures in extensional settings — A review, Earth Sci. Rev., 154, 14–28, doi:10.1016/j.earscirev.2015.11.014, 2016.
Fouke, B. W., Everts, A. W., Zwart, E. W. and Schlager, W.: Subaerial exposure unconformities on the Vercors carbonate platform (SE France) and their sequence stratigraphic significance, Geol. Soc. London, Spec. Publ., 104, 295–319, 1996.
Fournier, F. and Borgomano, J.: Critical porosity and elastic properties of microporous mixed carbonate-siliciclastic rocks, Geophysics, 74(2), E93–E109, doi:10.1190/1.3043727, 2009.
Fournier, F., Leonide, P., Biscarrat, K., Gallois, A., Borgomano, J. and Foubert, A.: Elastic properties of microporous cemented grainstones, Geophysics, 76(6), E211–E226, doi:10.1190/geo2011-0047.1, 2011.
Gattacceca, J., Deino, A., Rizzo, R., Jones, D. S., Henry, B., Beaudoin, B. and Vadeboin, F.: Miocene rotation of Sardinia: New paleomagnetic and geochronological constraints and geodynamic implications, Earth Planet. Sci. Lett., 258(3–4), 359–377, doi:10.1016/j.epsl.2007.02.003, 2007.

Gaviglio, P., Bekri, S., Vandycke, S., Adler, P. M., Schroeder, C., Bergerat, F., Darquennes, A. and Coulon, M.: Faulting and deformation in chalk, J. Struct. Geol., 31(2), 194–207, doi:10.1016/j.jsg.2008.11.011, 2009.
Gisquet, F., Lamarche, J., Floquet, M., Borgomano, J., Masse, J. P. and Caline, B.: Three-dimensional structural model of composite dolomite bodies in folded area (upper Jurassic of the Etoile massif, southeastern France), Am. Assoc. Pet. Geol. Bull., 97(9), 1477–1501, doi:10.1306/04021312016, 2013.
Godet, A., Bodin, S., Föllmi, K. B., Vermeulen, J., Gardin, S., Fiet, N., Adatte, T., Berner, Z., Stüben, D. and van de Schootbrugge, B.: Evolution of the marine stable carbon-isotope record during the early Cretaceous: A focus on the late Hauterivian and Barremian in the Tethyan realm, Earth Planet. Sci. Lett., 242(3–4), 254–271, doi:10.1016/j.epsl.2005.12.011, 2006.
Guendon, J.-L. and Parron, C.: Les phenomenes karstiques dans les processus de la bauxitisation sur substrat carbonate. Exemple de gisement du sud est de la France, Ann. la Société Géologique Belgique, 108, 85–92, 1985.
Guieu, G.: Un exemple de tectonique tangentielle: l'évolution du cadre montagneux de Marseille, Bull. la Société Géologique Fr., 7 (T.IX N°, 610–630, 1967.
Guyonnet-Benaize, C., Lamarche, J., Masse, J. P., Villeneuve, M. and Viseur, S.: 3D structural modelling of small-deformations in poly-phase faults pattern. Application to the Mid-Cretaceous Durance uplift, Provence (SE France), J. Geodyn., 50(2), 81–93, doi:10.1016/j.jog.2010.03.003, 2010.
Hammond, K. J. and Evans, J. P.: Geochemistry, mineralization, structure, and permeability of a normal- fault zone, Casino mine, Alligator Ridge district, north central Nevada, 25, 717–736, doi:10.1016/S0191-8141(02)00060-3, 2003.
Heiland, J., Raab, S. and Potsdam, G.: Experimental Investigation of the Influence of Differential Stress on Permeability of a Lower Permian (Rotliegend) Sandstone Deformed in the Brittle Deformation, Phys. Chem. earth, 26(1), 33–38, doi:10.1016/S1464-1895(01)00019-9, 2001.
Hodson, K. R., Crider, J. G. and Huntington, K. W.: Temperature and composition of carbonate cements record early structural control on cementation in a nascent deformation band fault zone: Moab Fault, Utah, USA, Tectonophysics, 690, 240–252, doi:10.1016/j.tecto.2016.04.032, 2016.
Hollis, C., Vahrenkamp, V., Tull, S., Mookerjee, A. and Taberner, C.: Pore system characterisation in heterogeneous carbonates: An alternative approach to widely-used rock-typing methodologies, Mar. Pet. Geol., 27(4), 772–793, doi:10.1016/j.marpetgeo.2009.12.002, 2010.
Kaminskaite, I., Fisher, Q. J. and Michie, E. A. H.: Microstructure and petrophysical properties of deformation bands in high porosity carbonates, J. Struct. Geol., 119(November 2018), 61–80, doi:10.1016/j.jsg.2018.12.001, 2019.
Kim, Y. S., Peacock, D. C. P. and Sanderson, D. J.: Fault damage zones, J. Struct. Geol., 26(3), 503–517, doi:10.1016/j.jsg.2003.08.002, 2004.
Knipe, R. J.: The influence of fault zone processes and diagenesis on fluid flow, Diagenes. basin Dev. AAPG Stud. Geol., 36, 135–154 [online] Available from: http://archives.datapages.com/data/specpubs/resmi1/data/a067/a067/0001/0100/0135.htm, 1993.
Knipe, R. J., Jones, G. and Fisher, Q. J.: Faulting, fault sealing and fluid flow in hydrocarbon reservoirs: an introduction, Geol. Soc. London, Spec. Publ., 147(1), NP LP-NP, doi:10.1144/GSL.SP.1998.147.01.21, 1998.
Lamarche, J., Lavenu, A. P. C., Gauthier, B. D. M., Guglielmi, Y. and Jayet, O.: Relationships between fracture patterns, geodynamics and mechanical stratigraphy in Carbonates (South-East Basin, France), Tectonophysics, 581, 231–245, doi:10.1016/j.tecto.2012.06.042, 2012.
Lambert, L., Durlet, C., Loreau, J. P. and Marnier, G.: Burial dissolution of micrite in Middle East carbonate reservoirs (Jurassic-Cretaceous): Keys for recognition and timing, Mar. Pet. Geol., 23(1), 79–92, doi:10.1016/j.marpetgeo.2005.04.003, 2006.
Laubach, S. E., Eichhubl, P., Hilgers, C. and Lander, R. H.: Structural diagenesis, J. Struct. Geol., 32(12), 1866–1872, doi:10.1016/j.jsg.2010.10.001, 2010.
Lavenu, A. P. C., Lamarche, J., Gallois, A. and Gauthier, B. D. M.: Tectonic versus diagenetic origin of fractures in a naturally fractured carbonate reservoir analog [Nerthe anticline, Southeastern France, Am. Assoc. Pet. Geol. Bull., 97(12), 2207–2232, doi:10.1306/04041312225, 2013.
Leonide, P., Borgomano, J., Masse, J. and Doublet, S.: Relation between stratigraphic architecture and multi-scale heterogeneities in carbonate platforms: The Barremian – lower Aptian of the Monts de Vaucluse, SE France, Sediment. Geol., 265–266, 87–109, doi:10.1016/j.sedgeo.2012.03.019, 2012.
Léonide, P., Fournier, F., Reijmer, J. J. G., Vonhof, H., Borgomano, J., Dijk, J., Rosenthal, M., Van Goethem, M., Cochard, J. and Meulenaars, K.: Diagenetic patterns and pore space distribution along a platform to outer-shelf transect (Urgonian limestone, Barremian-Aptian, SE France), Sediment. Geol., 306, 1–23, doi:10.1016/j.sedgeo.2014.03.001, 2014.
Long, J. J. and Imber, J.: Geological controls on fault relay zone scaling, J. Struct. Geol., 33(12), 1790–1800, doi:10.1016/j.jsg.2011.09.011, 2011.

Lothe, A. E., Gabrielsen, R. H., Hagen, N. B. and Larsen, B. T.: An experimental study of the texture of deformation bands: effects on the porosity and permeability of sandstones, (1990), doi:10.1144/petgeo.8.3.195, 2002.
Lucia, F. J.: Origin and petrophysics of dolostone pore space, Geom. Petrog. Dolomite Hydrocarb. Reserv. Geol. Soc. London, Spec. Publ., 235, 141–155, doi:10.1144/GSL.SP.2004.235.01.06, 2004.
Machel, H. G.: Concepts and models of dolomitization: a critical reappraisal, Geol. Soc. London, Spec. Publ., 235(1), 7–63, doi:10.1144/GSL.SP.2004.235.01.02, 2004.
Machel, H. G., Cavell, P. A., Buschkuehle, B. E. and Michael, K.: Tectonically induced fluid flow in Devonian carbonate aquifers of the Western Canada Sedimentary Basin, Journal geochemical Explor., 70, 213–217, doi:10.1016/S0375-6742(00)00093-5, 2000.
Main, I. G., Kwon, O., Ngwenya, B. T. and Elphick, S. G.: Fault sealing during deformation-band growth in porous sandstone, Geology, 28(12), 1131–1134, doi:10.1130/0091-7613(2000)28<1131:FSDDGI>2.0.CO;2, 2000.
Masse, J.-P. and Philip, J.: Paléogéographie et tectonique du Crétacé moyen en Provence: révision du concept d'isthme durancien., Rev. Géographie Phys. Géologie Dyn., 18(1), 49–46, 1976.
Masse, J. P.: Les calcaires urgoniens de Provence (Valanginien-Aptien Inférieur) - Stratigraphie, paléontologie, paléoenvironnements et leur évolution, Marseille, Thèse de la Faculté des Sciences de Luminy (U2), 1976.
Masse, J. P. and Fenerci-Masse, M.: Carbonate production by rudist bivalves. The record of Late Barremian requieniid communities from Provence (SE France), Palaeogeogr. Palaeoclimatol. Palaeoecol., 234(2–4), 239–257, doi:10.1016/j.palaeo.2005.10.010, 2006.
Masse, J. P. and Fenerci Masse, M.: Drowning discontinuities and stratigraphic correlation in platform carbonates. The late Barremian-early Aptian record of southeast France, Cretac. Res., 32(6), 659–684, doi:10.1016/j.cretres.2011.04.003, 2011.
Matonti, C., Lamarche, J., Guglielmi, Y. and Marié, L.: Structural and petrophysical characterization of mixed conduit/seal fault zones in carbonates: Example from the Castellas fault (SE France), J. Struct. Geol., 39, 103–121, doi:10.1016/j.jsg.2012.03.003, 2012.
Micarelli, L., Benedicto, A. and Wibberley, C. A. J.: Structural evolution and permeability of normal fault zones in highly porous carbonate rocks, J. Struct. Geol., 28(7), 1214–1227, doi:10.1016/j.jsg.2006.03.036, 2006.
Molli, G., Cortecci, G., Vaselli, L., Ottria, G., Cortopassi, A., Dinelli, E., Mussi, M. and Barbieri, M.: Fault zone structure and fluid–rock interaction of a high angle normal fault in Carrara marble (NW Tuscany, Italy), J. Struct. Geol., 32(9), 1334–1348, doi:10.1016/j.jsg.2009.04.021, 2010.
Molliex, S., Bellier, O., Terrier, M., Lamarche, J., Martelet, G. and Espurt, N.: Tectonic and sedimentary inheritance on the structural framework of Provence (SE France): Importance of the Salon-Cavaillon fault, Tectonophysics, 501(1–4), 1–16, doi:10.1016/j.tecto.2010.09.008, 2011.
Moss, S. and Tucker, M. E.: Diagenesis of Barremian-Aptian platform carbonates (the Urgonian Limestone Formation of SE France): near-surface and shallow-burial diagenesis, Sedimentology, 42(6), 853–874, doi:10.1111/j.1365-3091.1995.tb00414.x, 1995.
Mozley, P. S. and Goodwin, L. B.: Patterns of cementation along a Cenozoic normal fault: a record of paleoflow orientations, Geology, 23(6), 539–542, doi:10.1130/0091-7613(1995)023<0539:POCAAC>2.3.CO;2, 1995.
Nelson, R.: Geologic Analysis of Naturally Fractured Reservoirs, second ed., 2001.
Ostwald, W.: Lehrbuch der allgemeinen Chemie, Verlag von Wilhelm Engelmann, Leipzig, 2, 909, 1886.
Philip, J.: Les formations calcaires à rudistes du Crétacé supérieur provençal et rhodanien, Thèse de Doctorat, Université de Provence (Marseille), 1970.
Le Pichon, X., Bergerat, F. and Roulet, M.-J.: Plate kinematics and tectonics leading to the Alpine belt formation; A new analysis, Geol. Soc. Am., 218(March 1986), 111–131, doi:10.1130/SPE218-p111, 1988.
Pichon, X. Le, Rangin, C., Hamon, Y., Loget, N., Lin, J. Y., Andreani, L. and Flotte, N.: Geodynamics of the france southeast basin, Bull. la Soc. Geol. Fr., 181(6), 477–501, doi:10.2113/gssgfbull.181.6.477, 2010.
Purser, B. H.: Sédimentation et diagenèse des carbonates néritiques récents, Les éléments de la sédimentation et de la diagenèse, Ed. Tech., 1, 366, 1980.
Reches, Z. and Dewers, T. A.: Gouge formation by dynamic pulverization during earthquake rupture, Earth Planet. Sci. Lett., 235(1–2), 361–374, doi:10.1016/j.epsl.2005.04.009, 2005.
Reid, R. P. and Macintyre, I. G.: Microboring Versus Recrystallization: Further Insight into the Micritization Process, J. Sediment. Res., 70(May), 24–28, doi:10.1306/2DC408FA-0E47-11D7-8643000102C1865D, 2000.
Roche, V.: Analyse structurale et géo-mécanique de réseau de failles du chaînon de La Fare les Oliviers (Provence), Univ. Montpellier 2, 45, 2008.
Rossetti, F., Aldega, L., Tecce, F., Balsamo, F., Billi, A. and Brilli, M.: Fluid flow within the damage zone of the Boccheggiano extensional fault (Larderello-Travale geothermal field, central Italy): Structures, alteration and implications for hydrothermal mineralization in extensional settings, Geol. Mag., 148(4), 558–579,

797 doi:10.1017/S001675681000097X, 2011.
798 Saller, A. H. and Henderson, N.: Distribution of Porosity and Permeability in Platform Dolomites: Insight from the
799 Permian of West Texas: reply, Am. Assoc. Pet. Geol. Bull., 85, 530–532, doi:10.1306/090800850530, 2001.
800 Sallier, B.: Carbonates microporeux: influence de l'architecture du milieu poreux et de la mouillabilité sur les
801 écoulements diphasiques dans les réservoirs pétroliers, Univ. Genève., 2005.
802 Samankassou, E., Tresch, J. and Strasser, A.: Origin of peloids in Early Cretaceous deposits, Dorset, South England,
803 Facies, 51(1–4), 264–273, doi:10.1007/s10347-005-0002-8, 2005.
804 Séranne, M.: The Gulf of Lion continental margin (NW Mediterranean) revisited by IBS: an overview, Geol. Soc.
805 London, Spec. Publ., 156(1), 15–36, doi:10.1144/GSL.SP.1999.156.01.03, 1999.
806 Sibley, D. F. and Gregg, J. A. Y. M.: Classification of Dolomite Rock Texture, J. Sediment. Petrol., 57(6), 967–975,
807 doi:10.1306/212F8CBA-2B24-11D7-8648000102C1865D, 1987.
808 Sibson, R. H.: Crustal stress, faulting and fluid flow, Geol. Soc. London, Spec. Publ., 78(1), 69–84,
809 doi:10.1144/GSL.SP.1994.078.01.07, 1994.
810 Sibson, R. H.: Structural permeability of fluid-driven fault-fracture meshes, J. Struct. Geol., 18(8), 1031–1042,
811 doi:10.1016/0191-8141(96)00032-6, 1996.
812 Sinisi, R., Petrullo, A. V., Agosta, F., Paternoster, M., Belviso, C. and Grassa, F.: Contrasting fault fluids along high-
813 angle faults: a case study from Southern Apennines (Italy), Tectonophysics, 690(PartA), 206–218,
814 doi:10.1016/j.tecto.2016.07.023, 2016.
815 Solum, J. G. and Huisman, B. A. H.: Toward the creation of models to predict static and dynamic fault-seal potential
816 in carbonates, Pet. Geosci., 23(1), 70–91, doi:10.1144/petgeo2016-044, 2016.
817 Solum, J. G., Davatzes, N. C. and Lockner, D. A.: Fault-related clay authigenesis along the Moab Fault: Implications
818 for calculations of fault rock composition and mechanical and hydrologic fault zone properties, J. Struct. Geol., 32(12),
819 1899–1911, doi:10.1016/j.jsg.2010.07.009, 2010.
820 Storti, F., Billi, A. and Salvini, F.: Particle size distributions in natural carbonate fault rocks: Insights for non-self-
821 similar cataclasis, Earth Planet. Sci. Lett., 206(1–2), 173–186, doi:10.1016/S0012-821X(02)01077-4, 2003.
822 Swart, P. K.: The geochemistry of carbonate diagenesis: The past, present and future, Sedimentology, 62(5), 1233–
823 1304, doi:10.1111/sed.12205, 2015.
824 Tempier, C.: Modèle nouveau de mise en place des structures provençales, Bull. la Soc. Geol. Fr., 3, 533–540,
825 doi:10.2113/gssgfbull.III.3.533, 1987.
826 Tondi, E.: Nucleation, development and petrophysical properties of faults in carbonate grainstones: Evidence from the
827 San Vito Lo Capo peninsula (Sicily, Italy), J. Struct. Geol., 29(4), 614–628, doi:10.1016/j.jsg.2006.11.006, 2007.
828 Triat, J.: Paléoaltérations dans le crétacé supérieur de Provence rhodanienne, Strasbourg: Institut de Géologie –
829 Université Louis-Pasteur., 1982.
830 Vincent, B., Emmanuel, L., Houel, P. and Loreau, J. P.: Geodynamic control on carbonate diagenesis: Petrographic
831 and isotopic investigation of the Upper Jurassic formations of the Paris Basin (France), Sediment. Geol., 197(3–4),
832 267–289, doi:10.1016/j.sedgeo.2006.10.008, 2007.
833 Volery, C., Davaud, E., Foubert, A. and Caline, B.: Shallow-marine microporous carbonatereservoir rocks in the
834 Middle East: relationship with seawater Mg/Ca ration and eustatic sea level, J. Pet. Geol., 32(October), 313–325,
835 doi:10.1111/j.1747-5457.2009.00452.x, 2009.
836 Volery, C., Davaud, E., Foubert, A. and Caline, B.: Lacustrine microporous micrites of the Madrid Basin (Late
837 Miocene, Spain) as analogues for shallow-marine carbonates of the Mishrif reservoir formation (Cenomanian to Early
838 Turonian, Middle East), Facies, 56(3), 385–397, doi:10.1007/s10347-009-0210-8, 2010.
839 Walsh, J. J., Watterson, J., Bailey, W. R. and Childs, C.: Fault relays, bends and branch-lines, 21(8–9), 1019–1026,
840 doi:10.1016/S0191-8141(99)00026-7, 1999.
841 Walsh, J. J., Bailey, W. R., Childs, C., Nicol, A. and Bonson, C. G.: Formation of segmented normal faults: a 3-D
842 perspective, 25, 1251–1262, doi:10.1016/S0191-8141(02)00161-X, 2003.
843 Wilkins, S. J., Naruk, S. J., Wilkins, S. J., International, S., Naruk, S. J. and International, S.: Quantitative analysis of
844 slip-induced dilation with application to fault seal, 1(1), 97–113, doi:10.1306/08010605177, 2007.
845 Woodcock, N. H., Dickson, J. A. D. and Tarasewicz, J. P. T.: Transient permeability and reseal hardening in fault
846 zones: evidence from dilation breccia textures, Geol. Soc. London, Spec. Publ., 270, 43–53, 2007.
847 Wu, G., Gao, L., Zhang, Y., Ning, C. and Xie, E.: Fracture attributes in reservoir-scale carbonate fault damage zones
848 and implications for damage zone width and growth in the deep subsurface, J. Struct. Geol., 118(February 2017), 181–
849 193, doi:10.1016/j.jsg.2018.10.008, 2019.
850 Zhang, Y., Schaubs, P. M., Zhao, C., Ord, A., Hobbs, B. E. and Barnicoat, A. C.: Fault-related dilation, permeability
851 enhancement, fluid flow and mineral precipitation patterns: numerical models, Geol. Soc. London, Spec. Publ., 299(1),
852 239–255, doi:10.1144/SP299.15, 2008.

853 Zhu, W. and Wong, T.-F.: The transition from brittle faulting to cataclastic flow: Permeability evolution, J. Geophys.
854 Res., 102(96), 3027–3041, doi:10.1029/96JB03282, 1997.
855

856